Near-Field Dynamics and Plume Dispersion after an On-Road Truck: Implication to Remote Sensing

Jingwei Xie[1], Chun-Ho Liu[1,*], Ziwei Mo[1], Yuhan Huang[2,3] and Wai-Chuen Mok[1,2]

[1]Department of Mechanical Engineering, The University of Hong Kong, Hong Kong

[2]Centre for Green Technology, School of Civil and Environmental Engineering, University of Technology Sydney, Australia

[3]Jockey Club Heavy Vehicle Emission Testing and Research Centre, Vocational Training Council, Hong Kong

Revised Manuscript

Ref. No.: STOTEN-D-20-09479

submitted

to

Science of the Total Environment

on

July 26, 2020

[*]*Corresponding author address:*

Chun-Ho LIU

Department of Mechanical Engineering

7/F, Haking Wong Building

The University of Hong Kong

Pokfulam Road, Hong Kong, CHINA

Tel: +852 3917 7901 / +852 9788 7951

Fax: +852 2858 5415

Email: liuchunho@graduate.hku.hk

https://aplhk.tech

Near-Field Dynamics and Plume Dispersion after an On-Road Truck: Implication to Remote Sensing

Jingwei Xie[1], Chun-Ho Liu[1], Ziwei Mo[1], Yuhan Huang[2,3] and Wai-Chuen Mok[1,2]

[1]Department of Mechanical Engineering, The University of Hong Kong, Hong Kong

[2]Centre for Green Technology, School of Civil and Environmental Engineering, University of Technology Sydney, Australia

[3]Jockey Club Heavy Vehicle Emission Testing and Research Centre, Vocational Training Council, Hong Kong

Abstract

Apart from the aerodynamic performance (efficiency and safety), the wake after an on-road vehicle substantially influences the tailpipe pollutant dispersion (environment). Remote sensing is the most practicable measures for large-scale emission control. Its reliability, however, is largely dictated by how well the complicated vehicular flows and instrumentation constraint are tackled. Specifically, the broad range of motion scales and the short sampling duration (less than 1 sec) are the most prominent ones. Their impact on remote sensing has not been studied. Large-eddy simulation (LES) is thus employed in this paper to look into the dynamics and the plume dispersion after an on-road heavy-duty truck at speed U_∞ so as to elucidate the transport mechanism, examine the sampling uncertainty and develop the remedial measures. A major recirculation of size comparable to the truck height h is induced collectively by the roof-level prevailing flows, side entrainment and underbody wall jet. The tailpipe is enclosed by dividing streamlines so the plume is carried back to the truck right after emission. The recirculation augments the pollutant mixing, resulting in a more homogeneous pollutant distribution together with a rather high fluctuating concentration (over 20% of the time-

averaged concentrations). The plume ascends mildly before being purged out of the major recirculation to the far field by turbulence, leading to a huge reduction in pollutant concentration (an order of magnitude) outside the near wake. In the far-field, the plume is higher than the tailpipe and disperses in a conventional Gaussian distribution manner. Under this circumstance, a sampling duration for remote sensing longer than h/U_∞ would be prone to underestimating the tailpipe emission.

Keywords: Dispersion models, Heavy-duty truck, Large-eddy simulation (LES), Remote sensing technology, Sampling inaccuracy, Tailpipe emission.

1. Introduction

Automobile emission is a major air pollutant source, especially in mega cities where vehicles and pedestrians are in close proximity (Anenberg et al. 2017). It poses a serious threat to human health that would reduce life expectancy and increase the incidence of disease, especially for susceptible populations such as infants and elderlies (Abdull et al. 2020). The World Health Organization (WHO) reported that 91% of the world population resided in places where the air quality did not reach the WHO guidelines in 2016 (WHO 2020). Moreover, it was estimated that 4.2 million premature deaths were related to ambient air pollution in the same year. Under this circumstance, deteriorating air quality has become a critical issue that has attracted global concern for years (Gong and Wang 2018; Huang et al. 2018). Source control is the most effective solution to air pollution, yet reliable methods to determine the tailpipe emissions from a large number of in-use vehicles are vital to enforcement (Owais 2019).

Various methods have been attempted, including the portable emission measurement system (PEMS), plume chasing, tunnel measurement, ambient measurement and remote sensing, to measure the real-world tailpipe emissions from in-use vehicles accurately (Huang et al. 2018). In PEMS, gas analysers are mounted onboard the target vehicle to sample the exhaust gases (Kang et al. 2017). It can trace the emissions of a single vehicle during the journey, including driving and idling. However, the measurement is costly and time-consuming (Davison et al. 2020). Plume chasing adopts a mobile platform of measurement devices to follow individual on-road vehicles. It is able to capture the emission characteristics in real-world driving conditions (Wen et al. 2019). Whereas, there exist speed limits for safety concern and finite distance apart for sampling accuracy (Huang et al. 2018). Tunnel measurement monitors the pollutant fluxes while vehicles are passing through a tunnel (Giechaskiel et al. 2015). It can sample a large number of vehicles in a short time but cannot differentiate the emission footprint from individuals (Mazzoleni et al. 2010). Roadside measurement is logistically convenient to measure the ambient air pollutant levels in the vicinity of busy traffic using stationary roadside sampling equipment (Ning et al. 2012). Apart from collective emission from vehicle fleet, the data are unavoidably affected by rapid changes of meteorology in local scale (Ning et al. 2012, Huang et al. 2018).

Among others, remote sensing is a well-established technique that has been successfully implemented for years (Cadle and Stephens 1994). Compared with the aforementioned methods, it can collect the emission data from a large ensemble of vehicles as well as data logging the information of individuals (Mazzoleni et al. 2010). In addition, it is most cost-effective in terms of coverage, deployment and manpower (Xie et al. 2004). Single, instantaneous pass-by measurement in short sampling duration (less than 1 sec), however, is prone to error that degrades the confidence and even ends up with false detections (Huang et al. 2018). In fact, the flows around an on-road vehicle is inherently three-dimensional (3D), exhibiting complicated dynamics such as separations, recirculations and longitudinal vortices

(Choi et al. 2014). The intermittency also imposes a technical challenge for airborne pollutant measurements, which would further impair on-road remote sensing (Zhang et al. 2015). Most studies have focused on the aerodynamic performance (for safety and control) of vehicles but not environmental performance such as the exhaust plume dispersion (Rohit et al. 2019). This study is an extension of our previous one (Huang et al. 2020) in which certain good practices of remote sensing, such as valid measurement range and time, were proposed. In this paper, we elaborate on the dynamics and the dispersion mechanism behind. Large-eddy simulation (LES) is employed to examine in detail the unsteady flows and transport after an on-road, heavy-duty truck. The outcome could help improve remote sensing implementation, strengthen environmental management as well as better protect the health of pedestrians and other stakeholders.

The wake after an on-road vehicle is broadly divided into two distinct regions, namely, the near-wake and the far field (Hucho 1987). The near-wake is characterized by the intensive (spanwise) recirculation immediately behind the vehicle body together with a pair of counter-rotating (streamwise) trailing vortices (Vino et al. 2005). They are initiated by several factors such as flow separation and wake pumping (Baker 2001) that subsequently affect the aerodynamic forces and moments experienced by the vehicle (Ahmed et al. 1985). These flow features play equally important roles in the transport processes for environmental concern (Ahmed 1981) but have been less studied. Vehicular pollutants right after tailpipe are diluted rapidly by the near-wake recirculation before detrainment (Wang et al. 2013). The far field, on the other hand, consists of general turbulence behaviours without discernible flow structures (Baker, 2001). Its plume dispersion is thus well predicted by the Gaussian theory, including CALINE (California Line Source Dispersion Model; Benson 1992), OSPM (Operational Street Pollution Model; Berkowicz 2000) and HIWAY Model (Rao and Keenan 1980). In view of the persistent recirculations, the near-wake dispersion deviates from the Gaussian distribution (Zhao et al. 2015). A mixing zone with uniform turbulence was used in Gaussian models to handle vehicular wake effects (Zhang and Batterman 2013), which, however, often under-predicted the concentrations (Kota et al. 2013). The Gaussian models also under-estimated the streamwise diffusion which is important to near-field dispersion (Xing and Brimblecombe 2018). Vehicle momentum suppresses dispersion but forces the pollutants following its trajectory (Pospisil et al. 2004). However, these transport processes are hardly simulated in the Gaussian models. Currently, a handful of statistical models have been developed for near-wake dispersion based on the Ahmed vehicle model only (Dong and Chan 2006). The conventional solution therefore must be interpreted cautiously to determine the pollutant concentrations in the near-wake of an on-road vehicle.

Near-wake recirculation is important to the entire mixing processes after an on-road vehicle because it determines the initial pollutant strength and configuration. Hence, there is a need to unveil the limitations of conventional Gaussian models (Clifford et al. 1997; Gosse et al. 2011). All along, Ahmed vehicle models have been commonly adopted for simulating real-life scenarios. In this study, a heavy-duty commercial truck, which is available on the market, is used instead to include the surface details in the calculation. It has the typical, square-back, in which the after-vehicle flows differ from those of a fast-back one (Hu et al. 2015). Massive flow separations and reattachments are observed at the truck while a large, 3D recirculation is formed downstream at the base (Choi et al. 2014). Near-wake dispersion is tightly coupled with the complicated flows so additional effort is made to analyse the transport processes. Likewise, the majority of far-field dispersion can be well characterized by simple nondimensionalization techniques but not those in the near wake within a few vehicle heights (Chang et al. 2009b).

In view of the inadequacy of the conventional Gaussian models for estimating near-wake dispersion, wind tunnel experiments and computational fluid dynamics (CFD) have been adopted to tackle the problems. Using wind tunnel measurements, Kanda et al. (2006) contrasted the plume dispersion behind a passenger car with that behind a truck, focusing on the relationship between velocity and pollutant concentrations. It was found that the presence of the vehicle body augments the pollutant dispersion significantly. Moreover, the pollutant distribution is closely related to the mean and fluctuating velocities around the vehicle. Gosse et al. (2011) also employed wind tunnel measurements to study the dispersion after a simplified car model, considering the possibility of chemical reactions between vehicular emissions and the ambient atmospheric constituents. Although wind tunnel experiments are powerful tools for dispersion studies, it hardly captures the fast, transient processes after a moving bluff body in detail, such as the wake dynamics after an on-road vehicle. The one single uncontrollable or unpredictable factor would further induce uncertainty (Carpentieri et al. 2012). CFD, on the other hand, enables a refined spatio-temporal resolution of the flows as well as transport processes. It is therefore commonly used to diagnose the fundamental physics (Cheng and Liu 2011). Among CFD approaches, LES is appealing for studying the transient phenomena of fluid dynamics (Lesieur et al. 2018). It explicitly solves most of the conservation of momentum, mass and energy while modelling small portions of Reynolds stresses and pollutant fluxes at reasonable computation resources.

~~This section outlines the background of the problems and reviews the literature. The mathematical model and boundary conditions (BCs) are recorded in the next section. Results, including the flows, turbulence and dispersion, are reported in Section 3. The implication for remote sensing is discussed in Section 4. The conclusion is drawn in Section 5.~~

2. Methodology

2.1 Governing Equations

In this paper, the LES is conducted by the open-source CFD code OpenFOAM 6 (Weller et al. 1998). The flows are assumed incompressible and isothermal because buoyancy effect is limited to the proximity of tailpipes (Kanda et al., 2006). The filtered continuity

$$\frac{\partial \overline{u}_i}{\partial x_i} = 0 \tag{1}$$

and the filtered Navier-Stokes equation

$$\frac{\partial \overline{u}_i}{\partial t} + \frac{\partial}{\partial x_j}\overline{u}_i\overline{u}_j = -\frac{\partial \overline{\pi}}{\partial x_i} + \nu \frac{\partial^2 \overline{u}_i}{\partial x_j \partial x_j} - \frac{\partial \tau_{ij}}{\partial x_j} \tag{2}$$

are solved for the flows. Here, u_i is the velocity component in the i-direction, x_i the Cartesian coordinate, t the time and v the kinematic viscosity. The summation convention on repeated indices (i, j = 1, 2 and 3) applies. The overbar $\overline{\psi}$ denotes the spatial filtering employed to derive the LES resolved scales. The modified resolved-scale pressure

$$\overline{\pi} = \overline{p} + \frac{2}{3}k_{SGS} \tag{3}$$

where p is the kinematic pressure and k_{SGS} (= $\tau_{ii}/2$) the subgrid-scale (SGS) turbulence kinetic energy (TKE). The anisotropic part of SGS momentum flux τ_{ij} (= $\overline{u_i u_j} - \overline{u}_i\overline{u}_j$) is modelled by the Smagorinsky model (Smagorinsky 1963)

$$\tau_{ij} = -2\nu_{SGS}S_{ij} + \frac{2}{3}k_{SGS}\delta_{ij} \tag{4}$$

where ν_{SGS} (= $C_k k_{SGS}^{1/2}\Delta$) is the SGS kinematic viscosity, S_{ij} (= $\left[\partial\overline{u}_i/\partial x_j + \partial\overline{u}_j/\partial x_i\right]/2$) the rate-of-strain tensor, Δ (= $[\Delta_x\Delta_y\Delta_z]^{1/3}$) the filter width expressed as the cube root of the volume of hexahedral cell, δ_{ij} the Kronecker delta and C_k (= 0.07) a modelling constant. The SGS TKE conservation is handled by the one-equation TKE model (Schumann 1975)

$$\frac{\partial k_{SGS}}{\partial t}+\frac{\partial}{\partial x_i}k_{SGS}\bar{u}_i=2\nu_{SGS}S_{ij}S_{ij}+\left(\nu+\nu_{SGS}\right)\frac{\partial^2 k_{SGS}}{\partial x_i \partial x_i}-C_\varepsilon\frac{k_{SGS}^{3/2}}{\Delta} \quad (5)$$

where C_ε (= 1.05) is another modelling constant. The filtered pollutant transport equation

$$\frac{\partial\bar{\phi}}{\partial t}+\frac{\partial}{\partial x_i}\bar{\phi}\,\bar{u}_i=\frac{\nu+\nu_{SGS}}{Sc}\frac{\partial^2\bar{\phi}}{\partial x_i \partial x_i} \quad (6)$$

is solved for the dispersion where ϕ is the pollutant concentration and Sc (= 0.72) the Schmidt number. Carbon dioxide (CO_2) is taken as the pollutant so no chemical reaction is considered.

2.2 Computational Domain and Boundary Conditions

The model of the heavy-duty truck (Figure 1a) sizes 3.86h (length) × 0.89h (width) × 1.09h (height) while the computational domain (Figure 1b) is 31.8h (streamwise) × 3.9h (spanwise) × 10.3h (vertical). Here, h (= 3.27 m) is the height of the truck. Dirichlet BCs of constant wind speed U_∞ (= 10 m sec^{-1}) and zero pollutant $\bar{\phi}$ = 0 are prescribed at the inflow. The prevailing flows are thus in the streamwise x direction normal to the wind shield. The logarithmic law of the wall (log-law) is used to model the flow BCs on all the solid boundaries including the ground and the truck body. At the domain top and the spanwise extent, Neumann BCs ($\partial\bar{\psi}/\partial\vec{n}=0$ where $\vec{n}$ is the normal to the boundary surface) for both flows and dispersion are applied. A pollutant (point) source of size 20×10$^{-6}h^3$ with a constant emission rate $\dot{Q}$ is placed at the tailpipe exhaust (x = 0, y = 0, z = 0) to simulate vehicular pollutant. The effect of exhaust-induced turbulence is limited to the proximity of the tailpipe so the emission speed is not considered (Chan et al. 2001). An open BC ($\partial\bar{\phi}/\partial t+\bar{u}\,\partial\bar{\phi}/\partial x=0$) is applied at the outflow so all the pollutants are removed from the computational domain by the prevailing flows without any reflection. Neumann BCs for pollutants are adopted on all the solid boundaries. The Reynolds number based on the free-stream wind speeds U_∞ (characteristics velocity scale) and the truck height h (characteristic length scale) Re ($= U_\infty h/\nu$) is over 37,200 that is comparable to that in previous studies (Tunay et al. 2016). The characteristic pollutant concentration $\Phi_0 = \dot{Q}/U_\infty h^2$ represents roughly the far-field value.

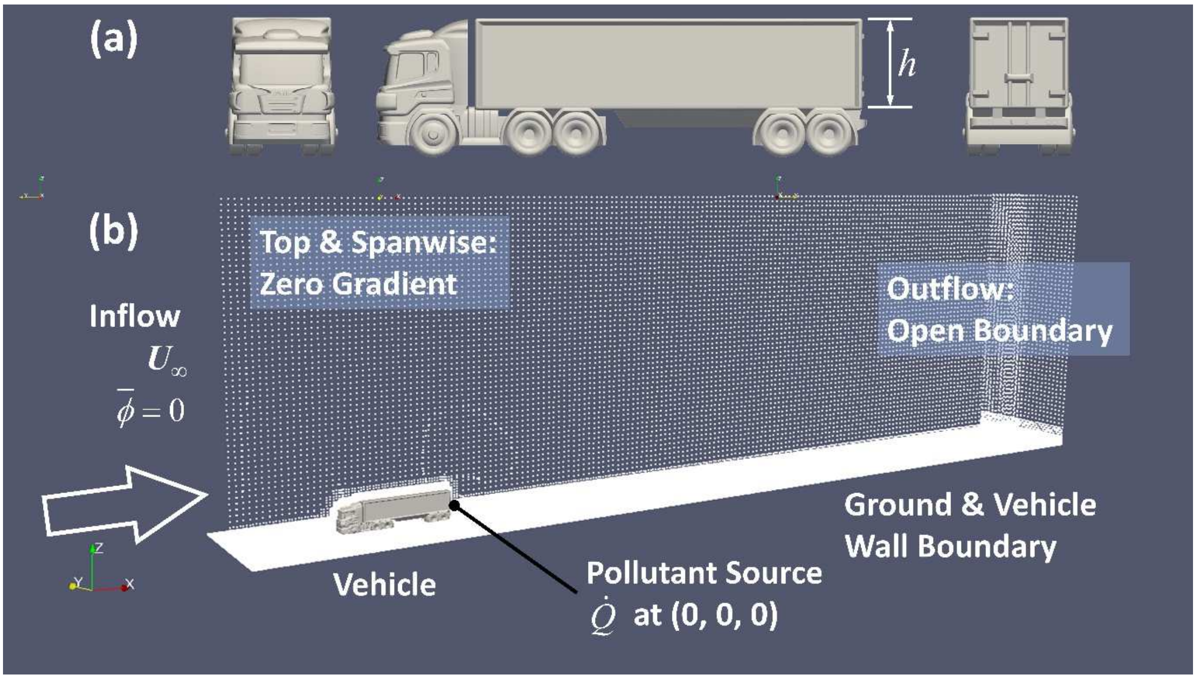

Figure 1. (a) Digital model of the heavy-duty truck together with (b) computational domain and boundary conditions.

2.3 Numerical Method

The spatial domain is discretized into 3.38 million unstructured hexahedra. The cells are refined towards the truck surfaces and the ground by the mesh generation utility *snappyHexMesh* (OpenFOAM 2018). The minimum and maximum cell volume is in the order of $10^{-7}h^3$ and $10^{-2}h^3$, respectively. The size of the cells is thus ranged from $0.005h$ to $0.2h$. The time-step increment is $\Delta t = 0.0013h/U_\infty$. The finite volume method (FVM) is used to solve the mathematical model. The implicit, second-order-accurate backward differencing is employed in the time integration. The gradient, divergence and Laplacian terms are integrated by the second-order-accurate Gaussian FVM based on the summation on cell faces. The pressure-implicit with splitting of operators (PISO) approach is used to handle the pressure-velocity coupling in incompressible flows. The preconditioned conjugate gradient (PCG) method is used to solve the symmetric equation system of pressure and the preconditioned bi-conjugate gradient (PBiCG) method is used to solve the asymmetric systems of other variables. The residual of the iterative solvers is less than 10^{-8} for converged solution. Equations are integrated in time for $30h/U_\infty$ to initialize the flows and dispersion. After pseudo-steady state, they are integrated for another $30h/U_\infty$ to compute the statistics. The data sampling time is long enough to ensure convergence of first- and second-order moments. In the following analyses, the angle brackets $<\psi>$ denote time average (mean) while the double prime ψ'' ($= \psi - <\psi>$) denotes the deviation from the time average $<\psi>$.

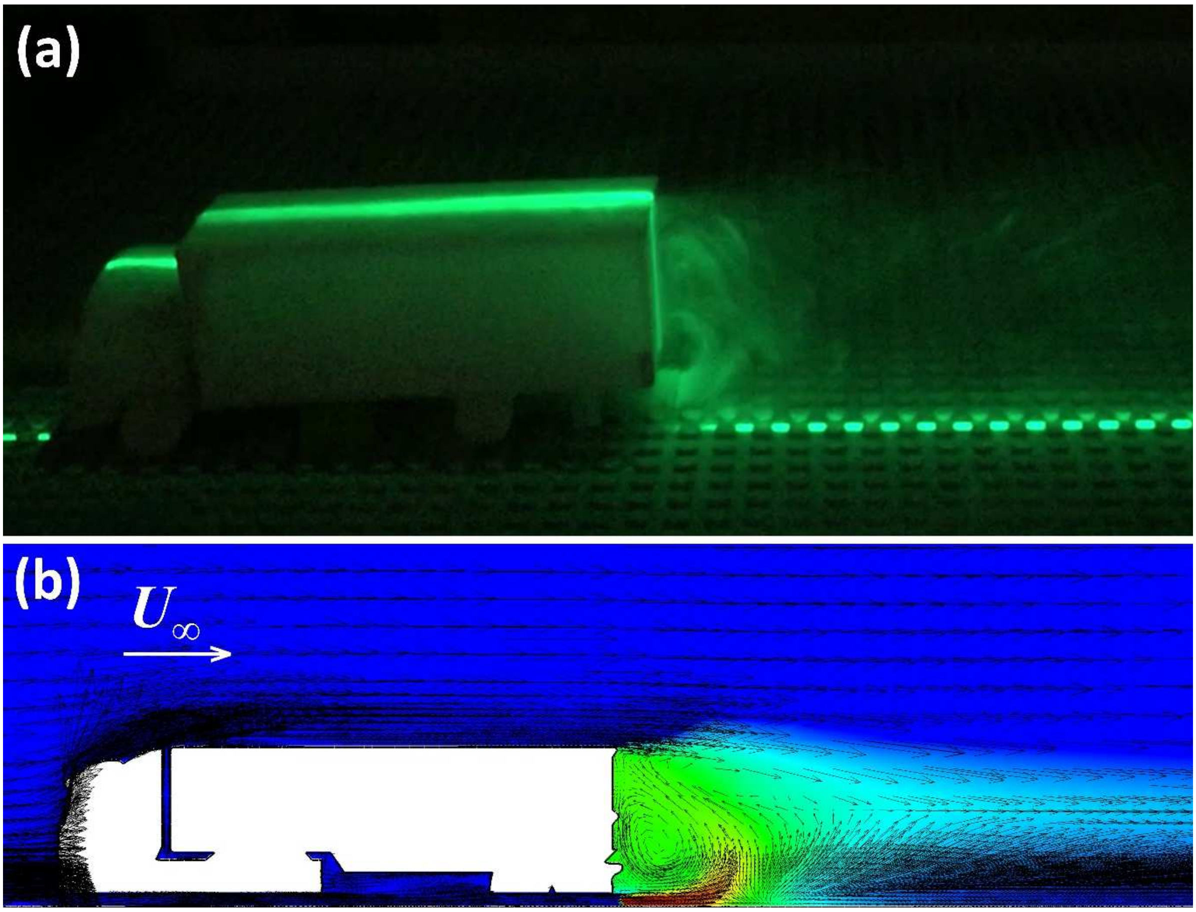

Figure 2. Visualization of the near-wake flows after a heavy-duty truck in: (a). previous wind tunnel experiment (Liu et al. 2019) and (b). the current LES.

3. Results

3.1 Flows

Both our previous wind tunnel visualization (Liu et al. 2019) and the current LES illustrate that the near wake after a truck consists of a major recirculation of size h (Figure 2). The recirculation (reverse flow) is highly 3D and emanates from the truck underbody toward the rear side. A similar flow pattern was reported schematically in laboratory experiments (Chang et al. 2009a). It is thus expected that the pollutant concentration is more homogeneous within the major recirculation. In this connection, a box model was proposed to determine the pollutant concentrations in the immediate vicinity of a roadway (Habegger et al. 1974) instead of the conventional Gaussian model. Over the truck, another counter-rotating, upper recirculation is developed, which is in line with the existing LESs (Chan et al. 2008; Minguez et al. 2008) as well as laboratory experiments (Wang et al. 2013; Sellappan et al. 2018). These recirculations are sensitive to vehicle shape, such as the rear slant angle, which tremendously affects the near-wake structure. We thus disentangle the pollutant transport mechanism from the dynamics to explore the technical difficulty of remote sensing.

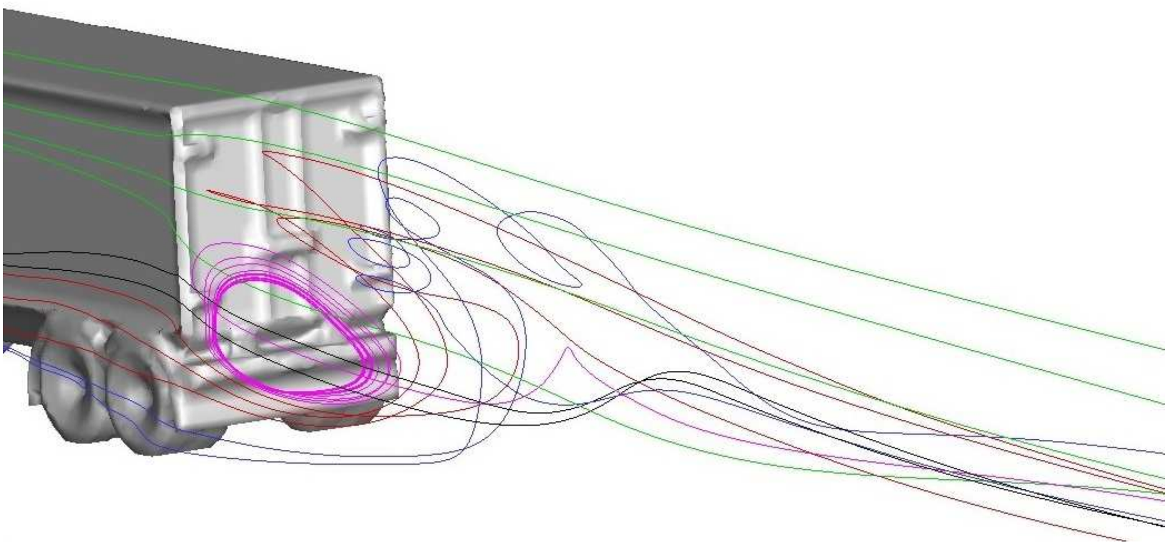

Figure 3. Streamlines illustrate the flow entrainment from the side into the near wake after the truck.

Although the upper recirculation is merely visualized in the wind tunnel experiment, the pollutant being emitted from the tailpipe is elevated to the upper part of the truck after the near wake (Figure 2a), which is in line with the current LES (Figure 2b). The flows entraining from the side are divided into three parts (Figure 3). The bottom part, which essentially climbs up a height of *h*, forms the outer region surrounding the major recirculation as well as initiates the upper recirculation. The top part is mainly driven by the prevailing flows that does not show noticeable meandering. The middle part immerses into the major recirculation. These structures align with those reported in the literature (McArthur et al. 2016).

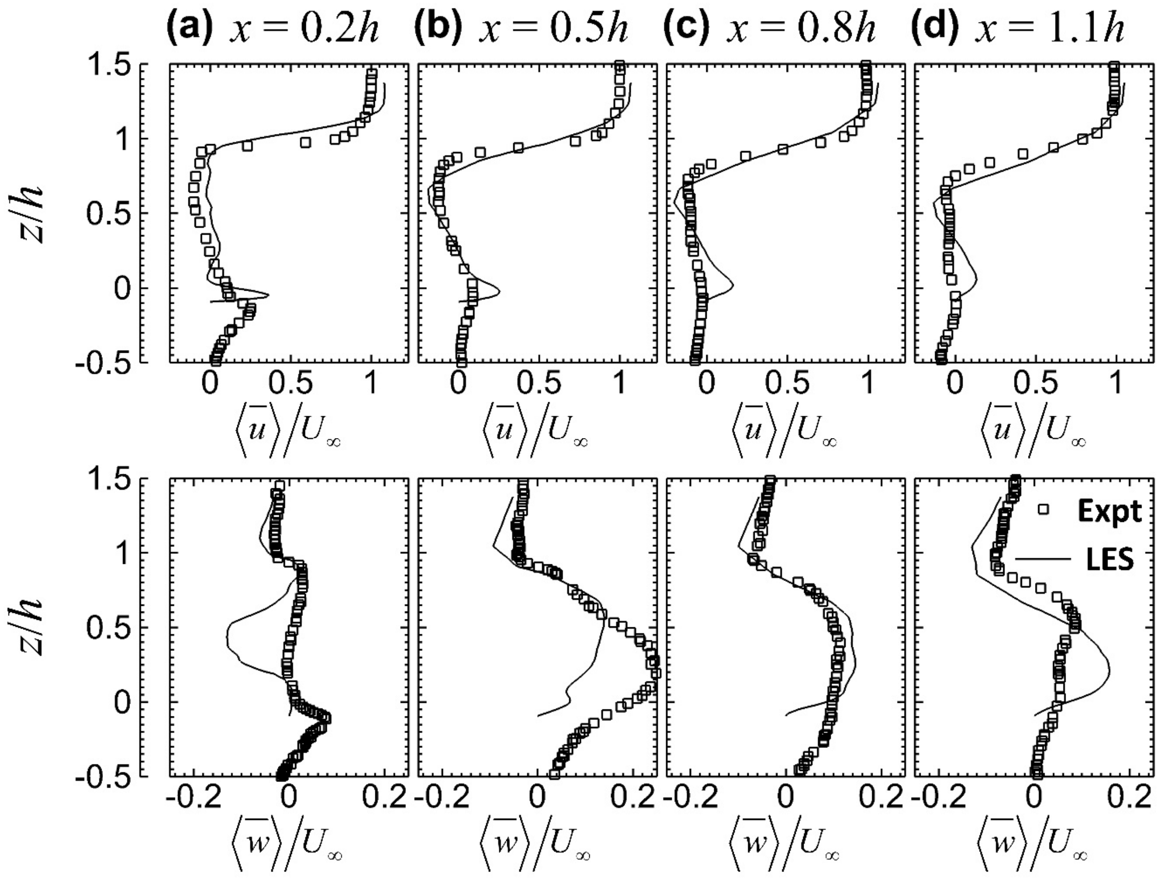

Figure 4. Vertical dimensionless profiles of mean streamwise $\langle \overline{u} \rangle / U_\infty$ and vertical $\langle \overline{w} \rangle / U_\infty$ velocities on the vertical (*x*-*z*) centre plane at $y = 0$ for x/h = (a). 0.2, (b). 0.5, (c). 0.8 and (d). 1.1. The experimental data are obtained from Lo and Kontis (2017).

Apart from the visualization, the current LES is validated by the wind tunnel results available in the literature (Lo and Kontis 2017). The near-wake velocity profiles obtained from the two solutions, especially the roof-level mixing layer, compare well with each other (Figure 4). The LES-calculated wall jet is slightly stronger than that of the wind tunnel. Discrepancy in the vertical flows is observed in the core of major recirculation. It could be attributed to the dissimilar vortex centres in the two studies. A strong wind shear (velocity difference $\Delta\langle\overline{u}\rangle \approx U_\infty$) and a mild wall jet ($0.1U_\infty \leq \Delta\langle\overline{u}\rangle \leq 0.3U_\infty$) are developed, respectively, about the roof level ($z \approx h$) and below the truck ($z \leq 0$). The upper flows are induced by the prevailing wind and pressure difference while the bottom wall jet is driven by the flows from the truck underbody. Moreover, mild downward ($-0.1U_\infty \leq \langle\overline{w}\rangle$) and upward ($\langle\overline{w}\rangle \leq 0.25U_\infty$) flows are observed at the top and bottom, respectively. These flow structures constitute the major recirculation, governing the rapid, early plume mixing. Close to the truck at $x = 0.2h$, the underbody wall jet is noticeable ($\langle\overline{u}\rangle = 0.3U_\infty$ and $\langle\overline{w}\rangle = 0.1U_\infty$; Figure 4a) that picks up the tailpipe emission. The flows then bend upwards ($\langle\overline{u}\rangle \leq 0.1U_\infty$ and $0.1U_\infty \leq \langle\overline{w}\rangle \leq 0.2U_\infty$) at $x = 0.5h$ (Figure 4b) and continue at $x = 0.8h$ (Figure 4c). The peaked vertical flows are further elevated to $z = 0.2h$ at $x = 1.1h$ (Figure 4d) close to the boundary of the major recirculation.

The truck models employed in the wind tunnel experiments and the current LES possess a few minor differences, such as the accessories on the bodies and the size of the truck, leading to the discrepancy in the wake structures. Nonetheless, they have the common square-back design so the near-wake flow structures are representative and generally agree with each other.

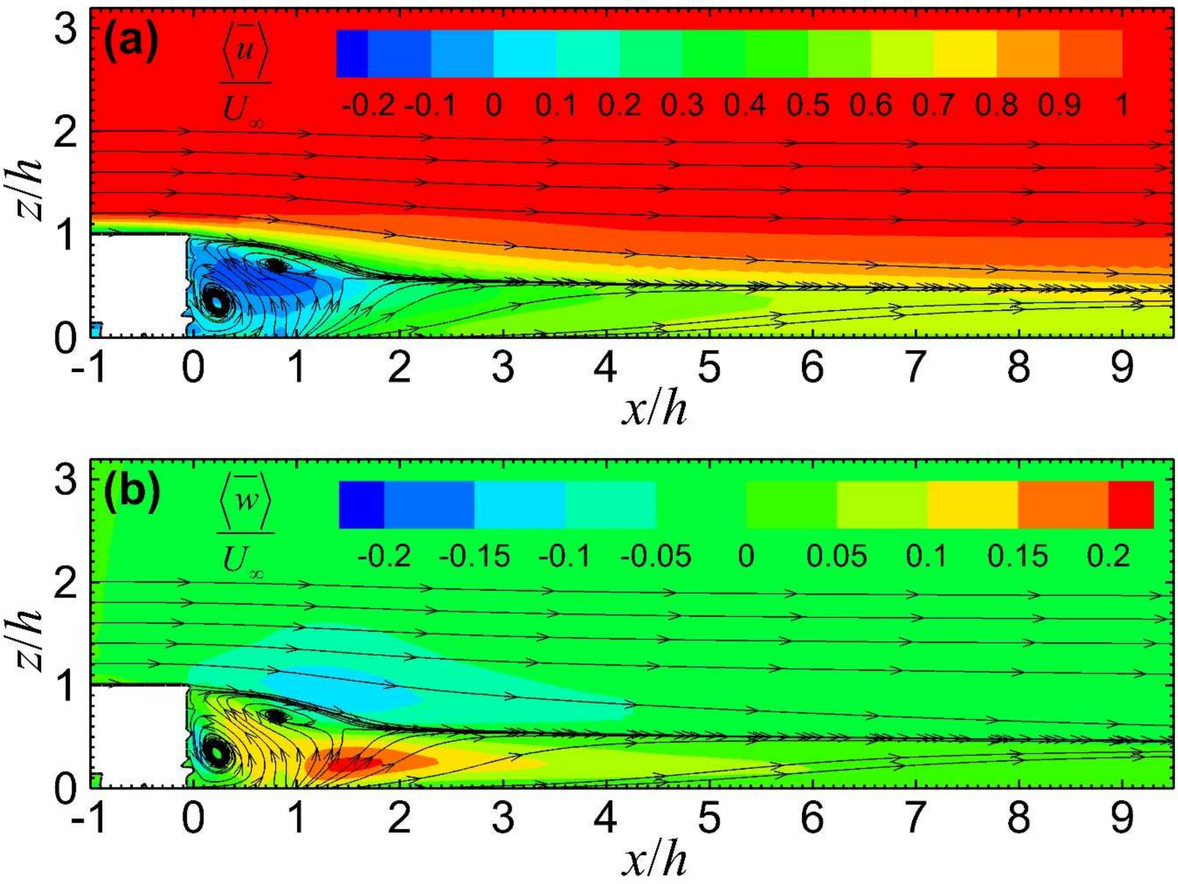

Figure 5. Shaded contours of dimensionless (a). streamwise $\langle \overline{u} \rangle / U_\infty$ and (b). vertical $\langle \overline{w} \rangle / U_\infty$ mean velocities on the vertical (x-z) centre plane at $y = 0$. Also shown are the streamlines.

The major and upper recirculations in the near wake ($x \leq h$) are depicted by the LES-calculated streamlines and velocities (Figure 5). Substantial reverse flows ($\langle \overline{u} \rangle \leq 0$) are observed in the near wake whose extremity ($\langle \overline{u} \rangle = -0.25U_\infty$) locates between the two counter-rotating recirculations ($x = 0.5h$, $z = 0.5h$). On top of the side entrainment, the prevailing flows descend mildly after the near wake ($x \geq h$), inducing the flow convergence at $z = 0.5h$ (Figure 5a). The convergence also serves as a group of dividing streamlines that partitions the vertical flows into the upward ($\langle \overline{w} \rangle > 0$) and downward ($\langle \overline{w} \rangle < 0$) regimes (Figure 5b). The roof-level downward flows ($0 \le x \le 3h$) locate over the upper recirculation, transferring momentum into the near wake. The upward flows are found below the dividing streamlines, rolling from the sides towards the truck behind the major recirculation while moving downstream. They are indeed largely induced by the low-level entrainment from the side (Figure 3).

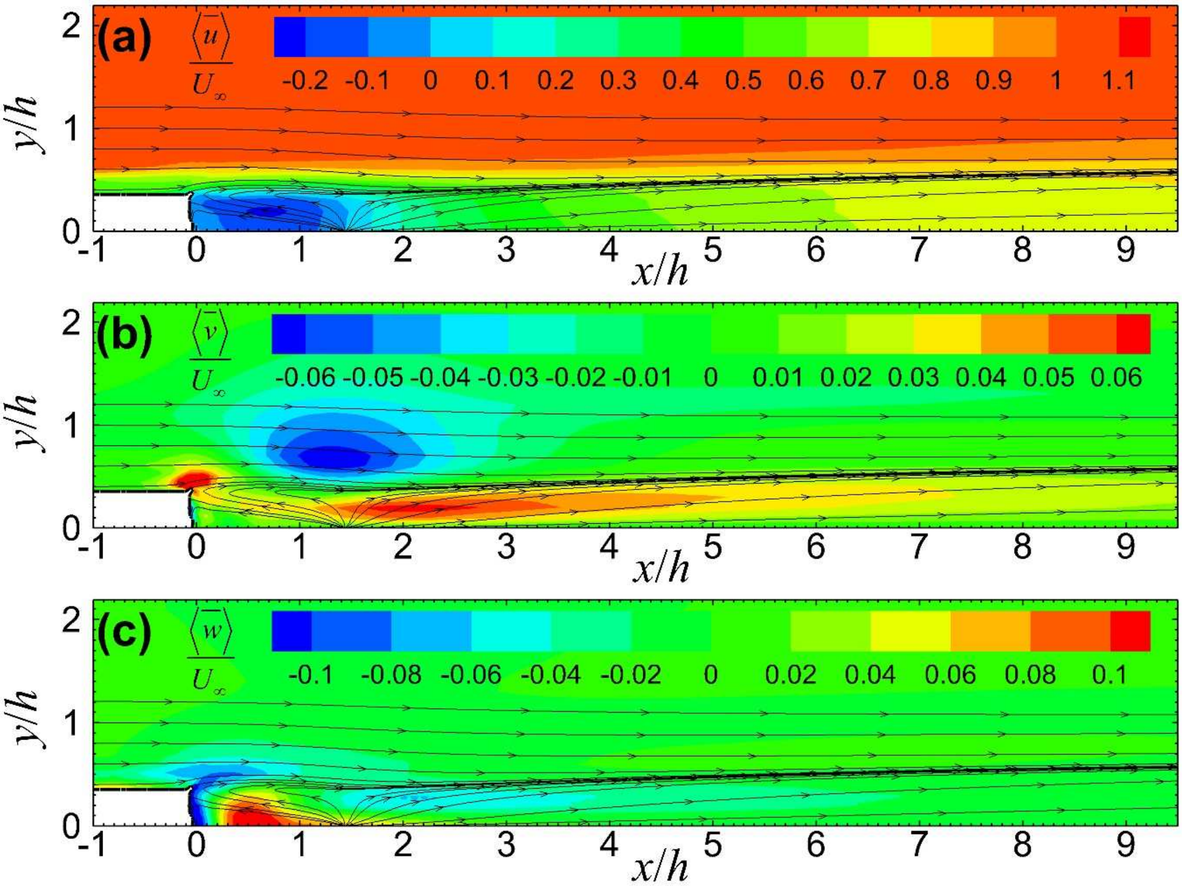

Figure 6. Shaded contours of dimensionless (a). streamwise $\langle \overline{u} \rangle / U_\infty$, (b). spanwise $\langle \overline{v} \rangle / U_\infty$ and (c). vertical $\langle \overline{w} \rangle / U_\infty$ mean velocities on the horizontal (*x*-*y*) plane at $z = 0.5h$. Also shown are the streamlines.

Flow convergence is also observed on the horizontal (*x*-*y*) plane at $z = 0.5h$, further characterizing the wake flows after the truck (Figure 6). The reverse flows ($\langle \overline{u} \rangle = -0.2U_\infty$) in the major recirculation are rather uniform (Figure 6a). Similar to the vertical flows on the *x*-*z* plane, the spanwise flows are partitioned into positive and negative on the horizontal (*x*-*y*) plane (Figure 6b). Apart from the flow separation at the truck edge before the wake, a mild, positive (outward) flow regime ($\langle \overline{v} \rangle = 0.06U_\infty$) is elongated ($1.5 \le x/h \le 3.5$) after the major recirculation, developing the flow convergence on the sides. On the other hand, negative spanwise flows ($\langle \overline{v} \rangle = -0.06U_\infty$) are found between the near wake and the far field ($x = 1.5h$). They are outside the convergence ($y \ge 0.4h$), which signifies the flow entrainment from the sides, though with weaker intensity (by 3 times) than the case of the vertical flows on the vertical centre plane (Figure 5). Both the time-averaged spanwise and vertical flows are towards the core at the same streamwise location ($0 \le x \le 3h$) that collectively enforce the flow convergence. Downward flows ($\langle \overline{w} \rangle = -0.1U_\infty$) are found after the truck edge on the horizontal plane (Figure 6c) that concur the three characteristic regimes discussed in Figure 3. After the major recirculation ($x \ge h$), the flows descend slightly ($\langle \overline{w} \rangle = -0.05U_\infty$), diminishing gradually in the streamwise direction.

3.2 Fluctuating Velocity

Turbulence $\langle u_i''u_i'' \rangle^{1/2}$ after the truck is quite isotropic except close to the ground surface near the boundary of major recirculation (Figure 7). The isotropy inside the major circulation is attributed to the recirculating flows that augments the homogeneous transport. They are rather small $\langle u_i''u_i'' \rangle^{1/2} \le 0.04U_\infty$ for $x \le 0.5h$ in the major recirculation. The streamwise ($\langle u''u'' \rangle^{1/2} = 0.14U_\infty$; Figure 7a) and spanwise ($\langle v''v'' \rangle^{1/2} = 0.16U_\infty$; Figure 7b) fluctuating velocities elevate close to the ground surface in $h \le x \le 2h$. These two peaks coincide with the boundary of major recirculation where the side entrainment drives the majority flow upward. Moreover, the underbody wall jet decelerates and bends upward. The local wind shear subsequently escalates the turbulence intensity.

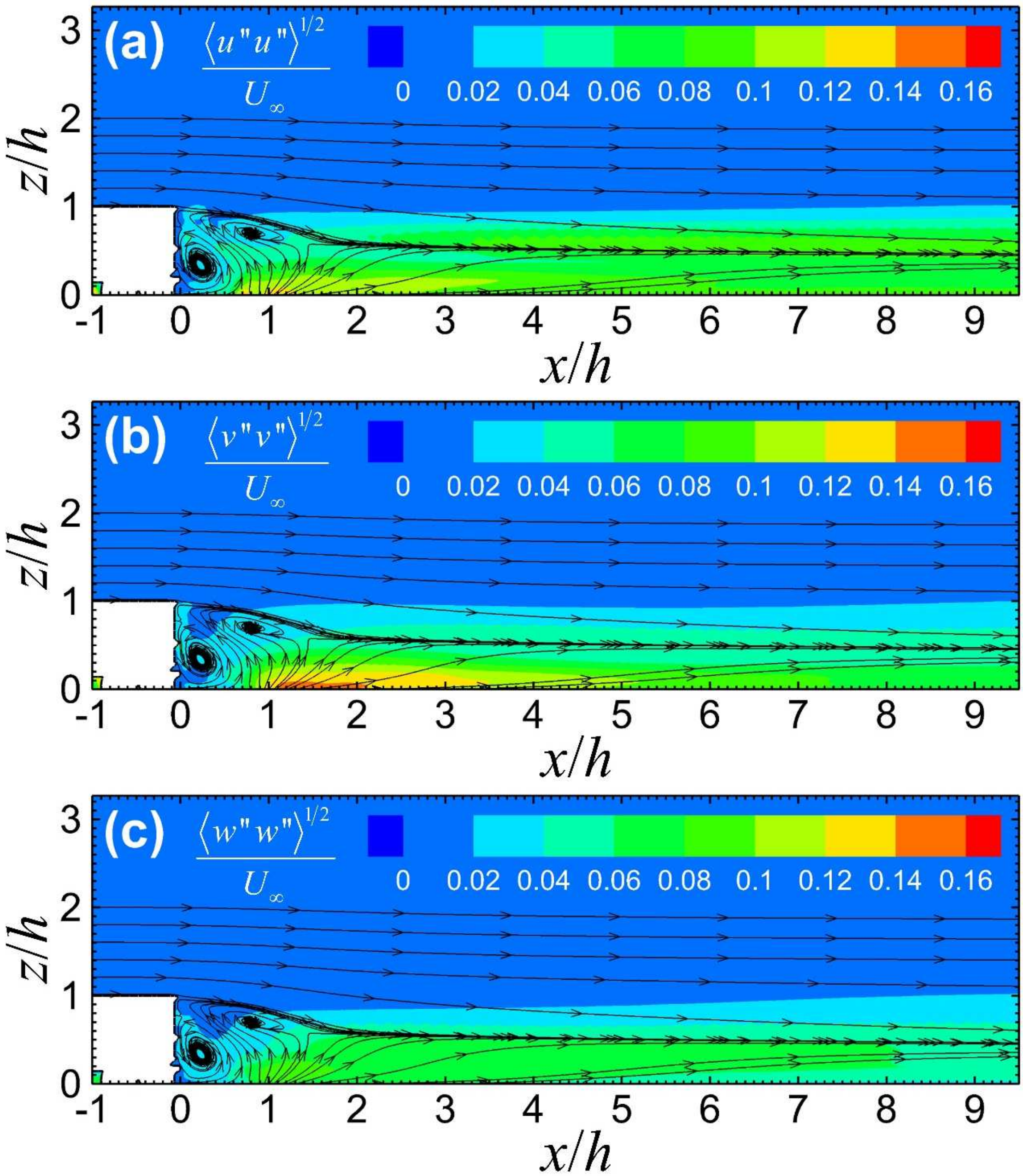

Figure 7. Shaded contours of dimensionless (a). streamwise $\langle u''u''\rangle^{1/2}/U_\infty$, (b). spanwise $\langle v''v''\rangle^{1/2}/U_\infty$ and (c). vertical $\langle w''w''\rangle^{1/2}/U_\infty$ fluctuating velocities on the vertical (x-z) centre plane at $y = 0$. Also shown are the streamlines.

It is noteworthy that the spanwise fluctuating velocity is even higher than its streamwise counterpart. The entrainment from the side is stronger than that from the top near the ground in $h \leq x \leq 2h$ (Figure 3). It concurs with the highly 3D-structured major recirculation. The flows are largely in the spanwise (inward) direction so is the peaked fluctuating velocity. Unlike the other two components, the vertical fluctuating velocity does not have a noticeable ground-level maximum but a rather uniform one $\langle w''w''\rangle^{1/2} = 0.06U_\infty$ in the entire far field (Figure 7c).

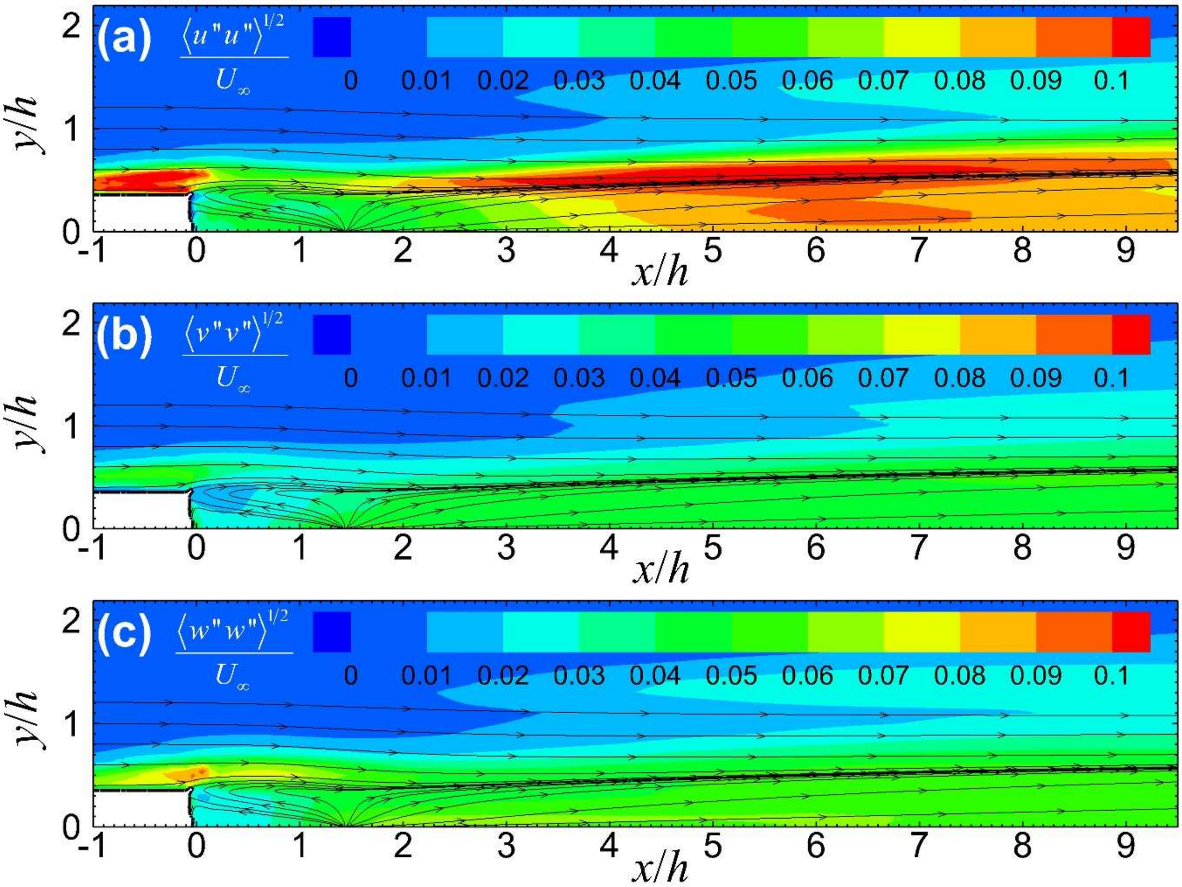

Figure 8. Shaded contours of dimensionless (a). streamwise $\langle u''u''\rangle^{1/2}/U_\infty$, (b). spanwise $\langle v''v''\rangle^{1/2}/U_\infty$ and (c). vertical $\langle w''w''\rangle^{1/2}/U_\infty$ fluctuating velocities on the horizontal (x-y) plane at $z = 0.5h$. Also shown are the streamlines.

The fluctuating velocities on the horizontal (x-y) plane at $z = 0.5h$ are augmented at the truck edge because of flow separation (Figure 8). In the entire range, the turbulence is less isotropic compared with that on the vertical (*x*-*z*) plane as shown in Figure 7. Generally, all the three components of fluctuating velocities in the far field are higher than those within the major recirculation (by two to three times). A faster spanwise transport process is thus expected. The peaked streamwise fluctuating velocity $\langle u''u''\rangle^{1/2} = 0.1U_\infty$, which doubles the other two components, is elongated on the side along the flow convergence for $x \geq 3h$ (in the far field; Figure 8a). It is apparently induced by the shear ($\Delta u \approx U_\infty/2$) between the wake and the prevailing flows (on the side). The local maximum subsequently induces the broad maximum of streamwise fluctuating velocity near the centre core. The spanwise $\langle v''v''\rangle^{1/2}$ (Figure 8b) and vertical $\langle w''w''\rangle^{1/2}$ (Figure 8c) fluctuating velocities, on the other hand, are rather uniform in the entire range. Another region of (mildly) elevated turbulence is found on the side for $y \geq h$ where the vortices are generated by the ground shear.

3.3. Pollutant Dispersion

The flows and turbulence discussed above form the basis to explain the plume characteristics on the vertical (*x*-*z*) centre plane at $y = 0$ (Figure 9). After being emitted from the tailpipe, the pollutant is driven by the major recirculation toward the truck (Figure 9a). The reverse flows are mainly driven by the side entrainment so the pollutant is mixed rapidly within the major recirculation. Pollutant overshot ($z \geq h$) is found in response to the upper recirculation and the elevated turbulence in the upper shear layer. The pollutant over the dividing streamlines is then diluted quickly by the prevailing flows at free-stream wind speed. Concurrently, the pollutant below the flow convergence is dispersed from the major recirculation to the upper recirculation at $x = 0.8h$, $z = 0.8h$ across the streamlines. Afterwards, it is carried downstream to the far field at a level ($z = h/2$ for $x \geq h$) higher than that of the tailpipe, resulting in the elevated plume trajectory. A sharp decrease in the pollutant concentration is thereafter observed between the major recirculation and the far field.

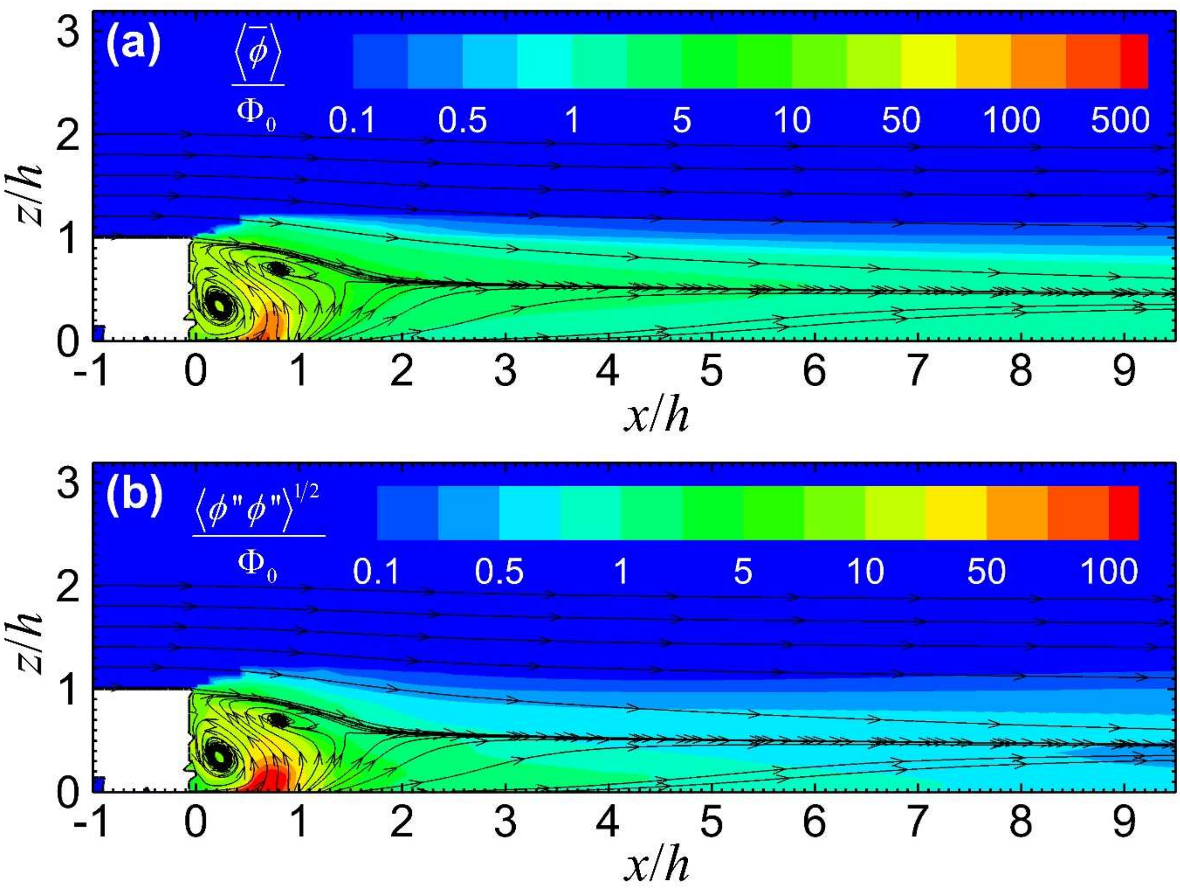

Figure. 9. Shaded contours of dimensionless (a). mean pollutant concentration $\langle\bar{\phi}\rangle / \Phi_0$ and (b). fluctuating pollutant concentration $<\phi''\phi''>^{1/2}/\Phi_0$ on the vertical (x-z) centre plane at $y = 0$. Also shown are the streamlines.

The maximum fluctuating pollutant concentration ($<\phi''\phi''>^{1/2} = 100\Phi_0$) is almost up to 20% of the mean pollutant concentration ($\langle\bar{\phi}\rangle = 250\Phi_0$) within the major recirculation that decreases along the plume trajectory (Figure 9b). It is caused by the reducing mean pollutant concentrations and the enhanced mixing in the major recirculation. The fluctuating pollutant concentration decreases to $<\phi''\phi''>^{1/2} \leq \Phi_0$ over the dividing streamlines. The prevailing flows dilute pollutants quickly, which in turn reduces both the mean and fluctuating concentrations. Below the dividing streamlines, on the other hand, the fluctuating pollutant concentration is higher ($1 \leq <\phi''\phi''>^{1/2}/\Phi_0 \leq 10$). Nonetheless it decreases gradually in the far field.

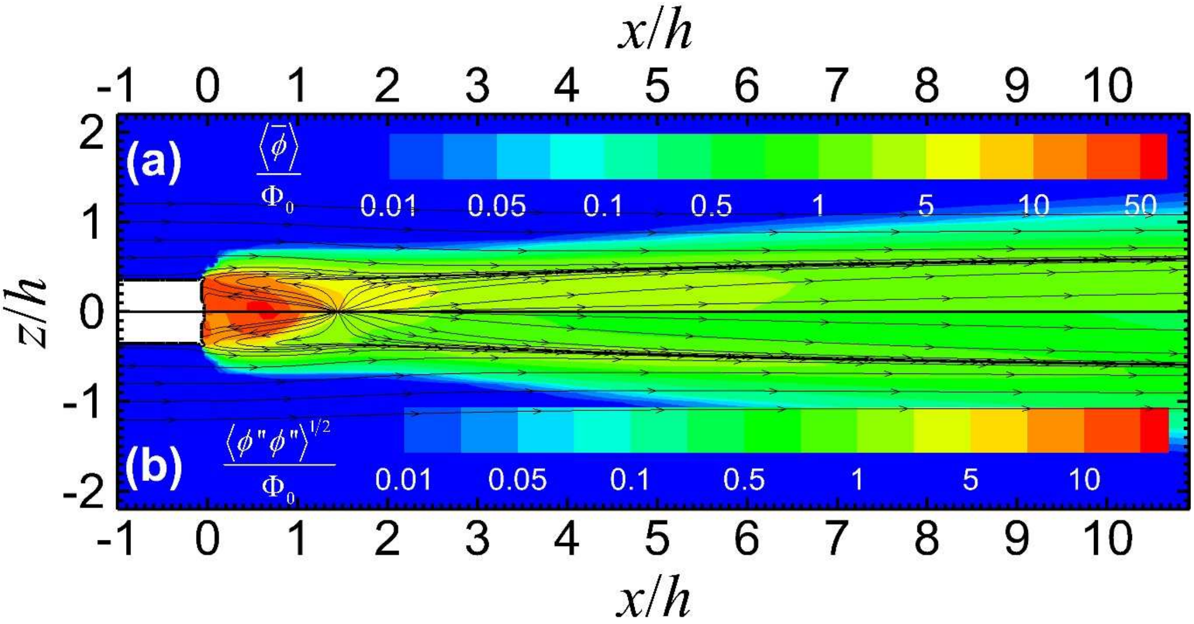

Figure 10. Shaded contours of dimensionless (a). mean pollutant concentration $\langle\overline{\phi}\rangle/\Phi_0$ and (b). fluctuating pollutant concentration $<\phi''\phi''>^{1/2}/\Phi_0$ on the horizontal (x-y) plane at $z = h/2$. Also shown are the streamlines.

Recurring on the horizontal (x-y) plane at $z = h/2$, most pollutants are trapped by the major recirculation after tailpipe emission (Figure 10). The homogeneous pollutant concentration within the major recirculation is clearly observed. The mean pollutant concentration in the major recirculation ($\langle\overline{\phi}\rangle \geq 50\Phi_0$) is higher than that in the far field ($\langle\overline{\phi}\rangle \approx \Phi_0$) by an order of magnitude. The major recirculation thus retains a large amount of tailpipe emission in a rather well-mixed manner. The dividing streamlines work together like a shelter, suppressing the pollutant removal from the major recirculation to the far field. Cross-streamline pollutant transport is governed by turbulence only that is much weaker than advection. A huge pollutant concentration gradient is thus developed between the major recirculation and the far field. In the far field, the local maximum of mean pollutant concentration shifts from the centre at $y = 0$ sideward to $y = 0.3h$, which deviates from the Gaussian theory. It is attributed to the off-centre streamwise pollutant advection that is explained in Section 3.4 below.

The fluctuating pollutant concentration ($<\phi''\phi''>^{1/2} \geq 25\Phi_0$) is elevated within the major recirculation (Figure 10b). It is as high as 50% of the time-averaged pollutant concentration ($\langle \overline{\phi} \rangle \approx 50\Phi_0$). Under this circumstance, the signal collected within the major recirculation, though strong, would be very noisy. In the far field, the peaked fluctuating pollutant concentration correlates tightly with the peaked mean pollutant concentration. It locates at $y = 0.5h$, displacing mildly from the peak of the mean pollutant concentration. The discrepancy could be explained by their dissimilar profiles. Note that fluctuating pollutant concentration is proportional to the gradient of the mean pollutant concentration.

When the *y*-*z* planes are located within the major recirculation (Figures 11a to 11c), the flows are characterized by two counter-rotating vortices. They are initiated by the near-wake, low-pressure zone which entrains the flows into the major recirculation. These pair of streamwise vortices were reported elsewhere (Lo and Kontis 2017). However, on the planes outside the major recirculation (Figures 11d to 11f), the key feature is the two counter-rotating trailing vortices on the *y*-*z* plane. It is also found that the upper shear layer gradually develops that interacts with the recirculations and the trailing vortices (modifies their flow directions and sizes). The two trailing vortices persist after $x \geq 1.75h$ that drive the flows further downstream. Apart from the trailing vortices, some small vortices are found near the ground which could be generated by ground-level shear.

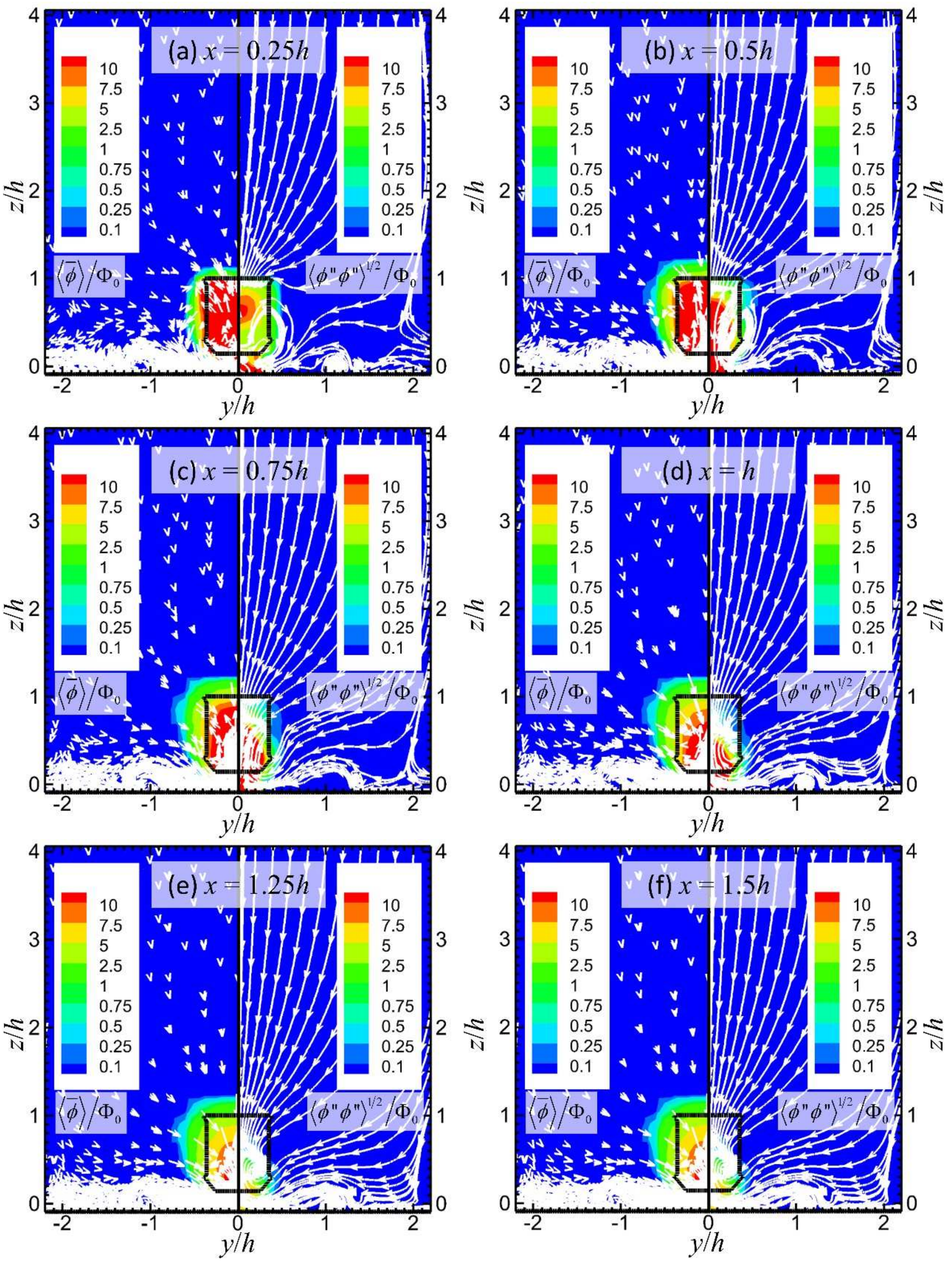

Figure 11. Shaded contours of dimensionless mean pollutant concentration $\langle\bar{\phi}\rangle/\Phi_0$ and fluctuating pollutant concentration $<\phi''\phi''>^{1/2}/\Phi_0$ on the vertical (y-z) plane at x/h = (a). 0.25; (b). 0.5; (c). 0.75; (d). 1; (e). 1,25 and (f). 1.5. Also shown are the flow vectors and the streamlines.

The tailpipe is located close to the plane at $x = 0.25h$ (Figure 11a) so there is a small region with elevated mean and fluctuating pollutant concentrations. The fluctuating pollutant concentration at $z = 0.7h$ is further intensified by the shear between the major and upper recirculations. The pollutant removal from the major recirculation is thus enhanced. The major recirculation mixes the pollutant rapidly (Figures 11b and 11c). The underbody wall jet drives the pollutant upwards so the mean pollutant concentration is rather uniform behind the truck (Figure 11b). The peaked time-averaged pollutant concentration then descends slightly after the major recirculation (Figure 11c). The coverage of fluctuating pollutant concentration at $x = 0.5h$ (Figure 11b) and $x = 0.75h$ (Figure 11c) is similar. It reflects the turbulent pollutant transport from the recirculations into the trailing vortices. In the far field ($x \geq h$), the pollutant is diluted quickly by the prevailing flows that is represented by the fast decreasing mean and fluctuating pollutant concentrations (Figure 11d and 11f). The mild descent of the upper shear layer is also observed (Figures 11d to 11e) that eventually converges for $x \geq 1.25h$ (Figures 11e and 11f). The peaked mean pollutant concentration remains at $z = 0.5h$. On the other hand, the peaked fluctuating pollutant concentration further descends (Figures 11e and 11f), resulting in a ground-level maximum.

3.4 Transport Mechanism

The streamwise mean pollutant flux on the vertical (x-z) centre plane at $y = 0$ shows elongated ($0 \leq x \leq 4h$), positive streamwise mean pollutant flux ($\langle\overline{\phi}\rangle\langle\overline{u}\rangle = 2\Phi_0 U_\infty$) over the dividing streamlines (Figure 12a). It in turn illustrates the mild advection of the pollutant overshot by the strong prevailing flows. In the major recirculation, the abandon tailpipe emission close to the unbody wall jet results in the maximum streamwise mean pollutant flux ($\langle\overline{\phi}\rangle\langle\overline{u}\rangle = 10\Phi_0 U_\infty$) near the ground at $x = h/2$. The flows reverse afterwards, leading to the minimum streamwise mean pollutant flux ($\langle\overline{\phi}\rangle\langle\overline{u}\rangle$ = -10$\Phi_0 U_\infty$) at z = h/2. These two equal-magnitude streamwise mean pollutant fluxes in opposite directions together with the local maximum vertical mean pollutant flux ($\langle\overline{\phi}\rangle\langle\overline{w}\rangle$ = 10$\Phi_0 U_\infty$) at the ground level (Figure 12b) develop the pollutant recirculation and the thorough mixing. Hence, the vehicular emission is escalated from the tailpipe to the upper recirculation, resulting in the rather uniform concentration within the major recirculation shown in Figures 9 and 10. The mean pollutant fluxes decrease gradually in the far field because of the diminishing vertical mean flow.

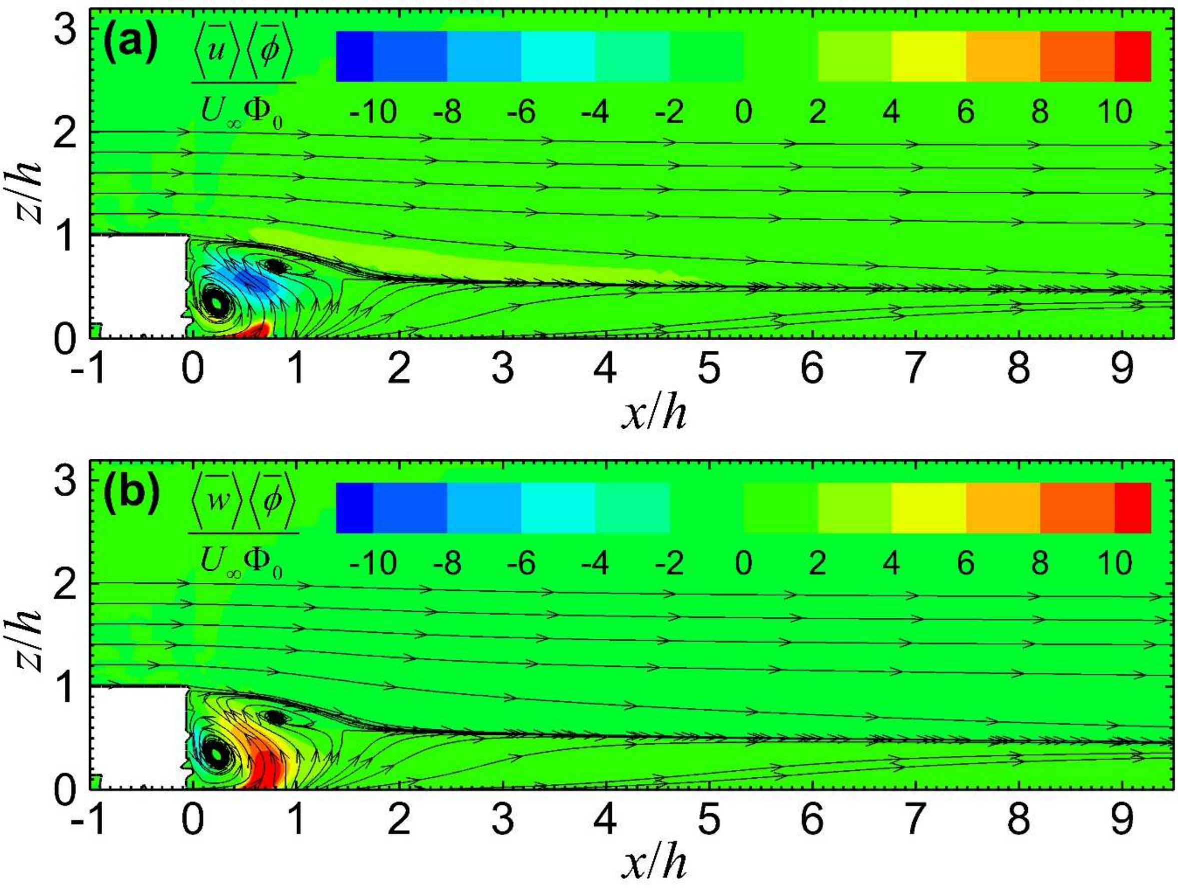

Figure 12. Shaded contours of dimensionless (a). streamwise $\langle\overline{u}\rangle\langle\overline{\phi}\rangle / U_\infty\Phi_0$ and (b) vertical $\langle\overline{w}\rangle\langle\overline{\phi}\rangle / U_\infty\Phi_0$ mean pollutant fluxes on the vertical (x-z) centre plane at y = 0. Also shown are the streamlines.

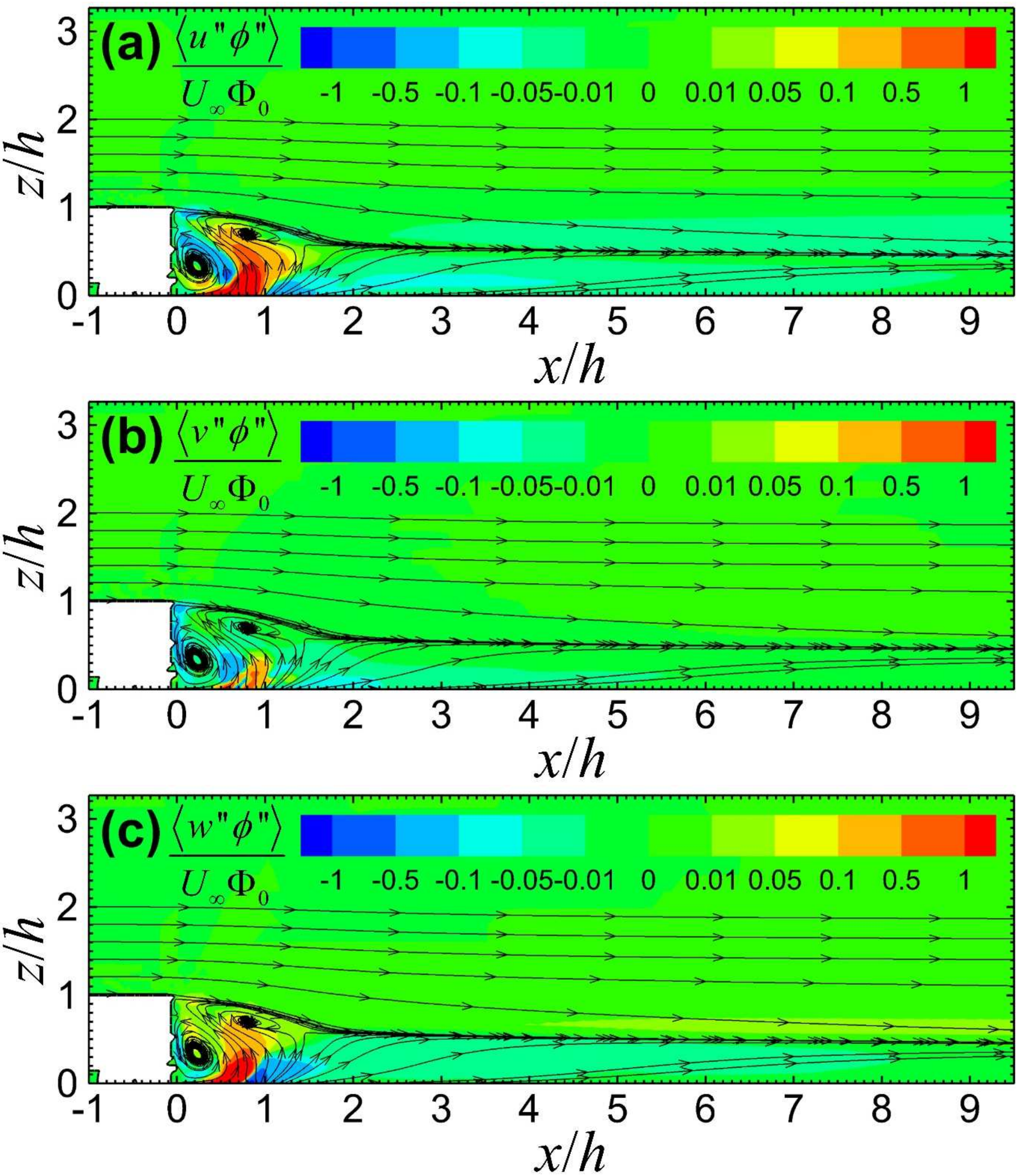

Figure 13. Shaded contours of dimensionless (a). streamwise $<\phi''u''>/U_\infty\Phi_0$, (b). spanwise $<\phi''v''>/U_\infty\Phi_0$ and (c). vertical $<\phi''w''>/U_\infty\Phi_0$ turbulent pollutant fluxes on the vertical (*x*-*z*) centre plane at $y = 0$. Also shown are the streamlines.

The turbulent pollutant fluxes $<\phi''u_i''>$ are largely negative within the major recirculation (Figure 13) that signify the rapid dilution by mean flows (pollutant concentrations decrease with increasing wind speeds). Their magnitudes ($|<\phi''u_i''>| \approx U_\infty\Phi_0$) are an order of magnitude smaller than those of mean pollutant fluxes ($\left|\left\langle \overline{u_i} \right\rangle \left\langle \overline{\phi} \right\rangle\right| \approx 10U_\infty\Phi_0$). Hence, the early plume mixing is fast and homogeneous, being dominated by advection.

A broad maximum of streamwise turbulent pollutant flux $<\phi''u''> = U_\infty\Phi_0$ is found in $0.5 \leq x/h \leq 1$. It is positive across the streamlines that suggests the majority turbulent pollutant removal from the major recirculation in the streamwise direction to the upper recirculation and to the far field (Figure 13a). The near-ground negative streamwise turbulent pollutant flux ($<\phi''u''> = -0.5U_\infty\Phi_0$) for $x \geq h$, on the other hand, depicts the pollutant dilution by prevailing flows. Another region of negative streamwise turbulent pollutant flux ($<\phi''u''> = -0.5U_\infty\Phi_0$) is developed within the major recirculation. The spanwise pollutant flux $<\phi''v''> = -0.1U_\infty\Phi_0$ is also negative for $x \geq h$ (Figure 13b). Both the streamwise and spanwise turbulent pollutant fluxes diminish for $x \geq 5h$. Small amounts of positive (upward) and negative (downward) vertical turbulent pollutant fluxes ($<\phi''w''> = \pm0.05\Phi_0U_\infty$) are found over and below the flow convergence, respectively (Figure 13c). These findings in turn suggest the crosswind pollutant transport in the far field which are analogous to those of Gaussian model along the plume trajectory. The far-field vehicular plume thus gradually resumes the Gaussian form. The vertical turbulent pollutant flux $<\phi''w''> = -0.5U_\infty\Phi_0$ is also negative for $x \approx h$ near the ground (Figure 13c) that is attributed to the dilution along ascending flows. It is positive along the major recirculation that indicates the turbulent pollutant transport from the major recirculation to the upper recirculation then the upper shear layer.

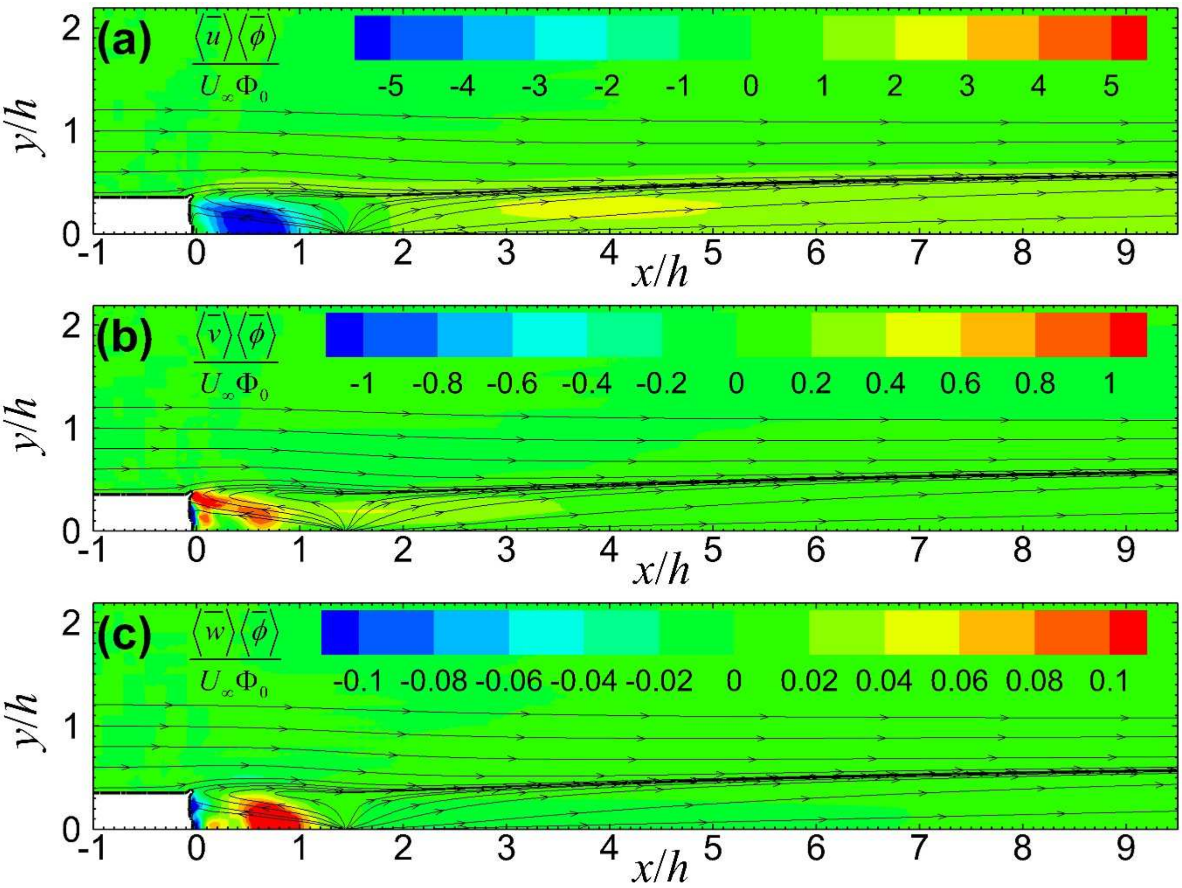

Figure 14. Shaded contours of dimensionless (a). streamwise $\langle\overline{u}\rangle\langle\overline{\phi}\rangle/U_\infty\Phi_0$, (b) spanwise $\langle\overline{v}\rangle\langle\overline{\phi}\rangle/U_\infty\Phi_0$ and (c). vertical $\langle\overline{w}\rangle\langle\overline{\phi}\rangle/U_\infty\Phi_0$ mean pollutant fluxes on the horizontal (x-y) plane at $z = 0.5h$. Also shown are the streamlines.

On the horizontal (x-y) plane at $z = h/2$ (Figure 14a), the streamwise mean pollutant flux is negative ($\langle\overline{\phi}\rangle\langle\overline{u}\rangle = -5\Phi_0 U_\infty$) and positive ($\langle\overline{\phi}\rangle\langle\overline{u}\rangle \geq \Phi_0 U_\infty$), respectively, in the major recirculation (reverse pollutant transport) and the far field (pollutant advection downstream). In particular, there is a local maximum $\langle\overline{\phi}\rangle\langle\overline{u}\rangle = 3\Phi_0 U_\infty$ at $x = 4h$, $y = 0.3h$ that is in line with the off-centre local maximum pollutant concentration presented before in Figure 10. Slightly elevated streamwise mean pollutant flux ($\langle\overline{\phi}\rangle\langle\overline{u}\rangle = 2\Phi_0 U_\infty$) is shown along the flow convergence because of the high speeds in the shear layer. On the other hand, the spanwise mean pollutant flux ($\langle\overline{\phi}\rangle\langle\overline{v}\rangle \geq 0.8\Phi_0 U_\infty$) is almost all positive (except very close to the truck) that widens the plume coverage (Figure 14b). Unlike its streamwise counterpart, the spanwise mean pollutant flux diminishes for $x \geq 5h$, overlapping with the dividing streamlines. The flows thereafter largely resume to the prevailing ones so the spanwise velocity is minimal. Within the major recirculation, positive vertical mean pollutant flux $\langle\overline{\phi}\rangle\langle\overline{w}\rangle = 0.1\Phi_0 U_\infty$ is observed in $0.5h \leq x \leq h$ and negative $\langle\overline{\phi}\rangle\langle\overline{w}\rangle = -0.1\Phi_0 U_\infty$ is limited to the truck base (Figure 14c). After the major recirculation, the vertical mean pollutant flux diminishes due to the prevailing horizontal flows. The far-field vertical pollutant transport is thus dominated by turbulence as discussed above in Figure 13. The extremities inside the major recirculation further support the reverse pollutant transport by advection toward the truck.

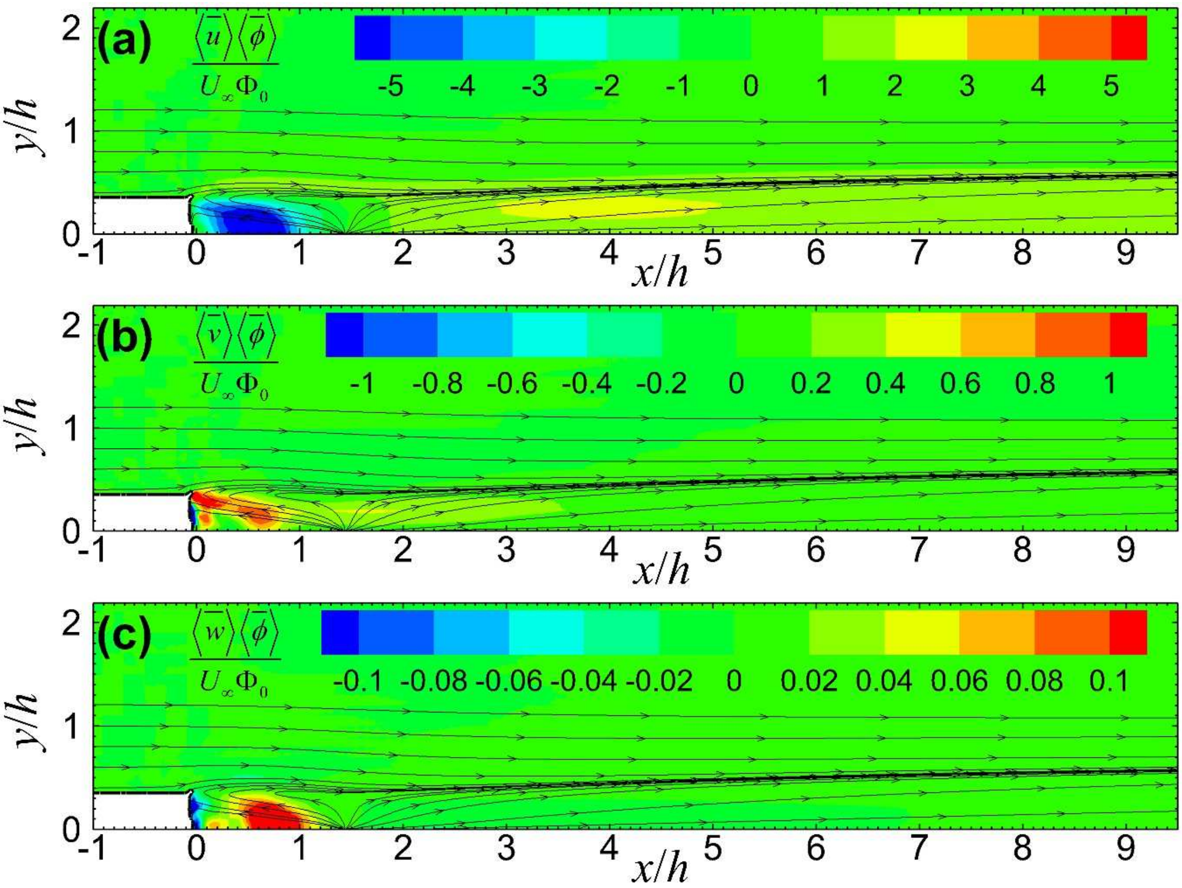

Figure 15. Shaded contours of dimensionless (a). streamwise $<\phi''u''>/U_\infty\Phi_0$, (b) spanwise $<\phi''v''>/U_\infty\Phi_0$ and (c). vertical $<\phi''w''>/U_\infty\Phi_0$ turbulent pollutant fluxes on the horizontal (x-y) plane at $z = h/2$. Also shown are the streamlines.

The turbulent pollutant fluxes $<\phi''u_i''>$ on the horizontal (x-y) plane at $z = h/2$ concur the mixing processes inside the major recirculation (Figure 15). The spanwise turbulent pollutant flux is smaller than the other two components (by 50%) because the major recirculation is rotating about the spanwise (y) axis. Within the near wake, the streamwise turbulent pollutant flux is largely positive which overlaps with the streamlines of reverse flows (dilution by advection). Only a tiny negative region is found close to the vertical (x-z) centre plane at $y = 0$. In the far field, a prolonged local minimum of streamwise turbulent pollutant flux ($<\phi''u''> \leq -0.04\Phi_0 U_\infty$) overlaps with the flow convergence (Figure 15a). This finding is in line with the elevated streamwise fluctuating velocity ($<u''u''>^{1/2} = 0.1U_\infty$) reported before in Figure 8a so the pollutant is diluted rapidly by prevailing flows. Turbulent transport, on the other hand, are illustrated clearly by the local maxima of spanwise turbulent pollutant flux $<\phi''v''> = 0.05\Phi_0 U_\infty$ across the streamlines at $x = 0.5h$ (Figure 15b) that carries the pollutant out of the major recirculation. Another elongated local maximum $<\phi''v''> = 0.04\Phi_0 U_\infty$ is observed in the far field that transports the pollutant across the flow convergence by turbulence as well. Its function is similar to that of Gaussian plume. The horizontal distribution of the vertical turbulent pollutant flux is alike its mean component as shown in Figure 14c. It gradually diminishes in the far field because of the prevailing flows (Figure 15c).

4. Discussion

The dynamics and transport mechanism discussed above facilitate our interpretation of tailpipe dispersion after an on-road vehicle. The distribution of mean pollutant concentration $\langle\overline{\phi}\rangle$ after a heavy-duty truck is quite different from that calculated by the Gaussian models. Within the major recirculation, the tailpipe emission is homogeneously mixed that results in a rather uniform mean pollutant concentration. Instead of an infinitely small pollutant point source, the size of the major recirculation is comparable to the height of truck h. Under this circumstance, the conventional Gaussian models are no longer applicable to the near-wake dispersion calculation. Besides, turbulent transport is required to remove the pollutant from the major recirculation to the far field. The pollutant concentration drops sharply in the streamwise direction and a noticeable concentration gradient is developed in-between.

After the major recirculation, the flows gradually resume to the prevailing ones so the Gaussian models are applicable. It is noteworthy that tailpipe emission is driven to a higher level ($z = h/2$) in the major recirculation before being removed to the upper recirculation and the far field. The plume trajectory is escalated but not at the tailpipe level so the emission height should be adjusted accordingly for $x \geq h$. The horizontal, crosswind plume dispersion also differs from the Gaussian theory. In view of the trailing vortices and the nonuniform pollutant advection, the maximum pollutant concentration is not along the centreline but shifts sideward to $y \approx 0.3h$. The peaks of fluctuating pollutant concentration are shifted as well.

The above findings help refine the practice of remote sensing. We reported before that a long sampling duration is unfavourable to remote sensing accuracy (Huang et al. 2020). The different diffusion coefficients of nitric oxide (NO) and CO_2 in air lead to different dispersion patterns. Under this circumstance, the assumption of constant NO-to-CO_2 ratio (the only parameter that is measured in remote sensing) is valid only in a short distance after the tailpipe exit. The ratio then reduces further downstream.

The aerodynamics after a heavy-duty truck reported in this paper shed some light on the reliable range of remote sensing (short sampling duration) as well. The LES results show that the major recirculation is enclosed by dividing streamlines. The pollutant removal from the major recirculation to the far field is governed by turbulent pollutant fluxes $\langle \phi'' u_i'' \rangle$

(across the streamlines), which, however, are much weaker (about an order of magnitude) than the mean pollutant flux $\langle\overline{\phi}\rangle\langle\overline{u}_i\rangle$. A noticeable difference in pollutant concentration is therefore developed. Despite the chemical composition, the pollutant concentrations drop sharply after the near wake (an order of magnitude). A long sampling duration would be prone to underestimating the tailpipe emission. Besides, the sharp drop in pollutant concentrations demands a higher detection sensitivity, which might stretch the capability of remote sensing to the limit. It in turn adversely affects the signal collected and measurement accuracy. The far-field plume trajectory is escalated from the tailpipe to a higher level ($z \approx h/2$) which is unfavourable to sampling confidence. In the current practice, remote sensing focuses at tailpipe level. Far-field plume ascent implies that accurate remote sensing would demand even more sensitive detection.

According to the above analysis, the best sampling range should be smaller than the major recirculation ($\leq h$) within which the pollutant mixing is more homogeneous and the concentration is more uniform. The corresponding sampling duration is therefore $\leq h/U_\infty$. Taking an on-road truck of size 3 m at speed 30 km hr^{-1} as an example, the sampling duration should be less than 0.4 sec. The current practice of remote sensing (0.5 sec) is marginally acceptable. The sampling time would be shortened for smaller vehicles (e.g. light-duty lorry) and faster driving speeds (e.g. 80 km hr^{-1} on most of the highways in Hong Kong). Apparently, slower driving speed would help improve the remote sensing accuracy. Otherwise, a shorter sampling duration is more favourable.

There exists another technical difficulty for shorter sampling duration. Unlike the usual turbulence intensities (approximately 10%), the current LES unveils that the fluctuating pollutant concentrations is up to 20% of the mean pollutant concentration in the major recirculation $(<\phi''\phi''>^{1/2} = 0.2\langle\overline{\phi}\rangle)$. It is thus expected that the signal data are noisy such that the conventional turbulence measurements should be implemented cautiously. One of the solutions could be prolonged sampling time, which, however, is unlikely practicable in remote sensing.

5. Conclusion

In this study, the flow and tailpipe pollutant dispersion after an on-road heavy-duty truck are examined by LES in detail. The current LES results agree well with our previous wind tunnel visualization and the wind profiles available in the literature. In line with previous studies, the flows after a truck can be divided into the near-wake and far-field regions. The near wake is composed of the major recirculation and the upper recirculation while the far field mainly consists of two trailing vortices. The upper shear layer not only induces the upper recirculation but also modifies the flows in the trailing vortices. It entrains into the trailing vortices finally.

Tailpipe emission is carried towards the truck following the major recirculation (reverse flows). Simultaneously, the pollutants are escalated from the tailpipe to a high level ($z \approx h/2$). In view of the rapid mixing, the pollutants are more homogeneous and the concentrations are more uniform within the major recirculation. In the far-field, the pollutant transport gradually follows the conventional Gaussian theory. However, the pollutant concentration is not peaked on the vertical (x-z) centre plane at $y = 0$ but shifted toward the dividing streamlines at $y = 0.3h$. Interestingly, substantial turbulent transport is found across those dividing streamlines. Generally, the pollutant transport by advection is 10 times larger than that by turbulence. It thus explains the thorough mixing in the major recirculation.

The current LES complements our previous finding that a shorter sampling duration favours remote sensing accuracy. In this paper, it is proposed that the sampling coverage should not extend beyond the major recirculation. Otherwise, the remote sensing signal would underestimate the pollutant concentrations. It is caused by the sharp drop in pollutant concentration (an order of magnitude) after the near wake. Nonetheless, the sampling time (0.5 sec) adopted in remote sensing nowadays is marginally acceptable.

Turbulence, especially within the shear layers from two sides of the truck and the region directly behind the recirculation, disperses the pollutant outside the recirculation. The trailing vortices can further elevate the pollutant to the level $z = 0.5h$ but the upper shear layer suppresses pollutant from being driven further upward over the dividing streamlines. Most pollutant in the far field is trapped by the trailing vortices and is transported downstream. Concurrently, the turbulence induced by the upper shear layer and trailing vortices disperse the pollutant within the vortices upwards and downwards, separately. The strong turbulence in the region between the trailing vortices and the mean flows also transports pollutant in the spanwise direction. Moreover, the turbulence induced by the trailing vortices leads to reverse pollutant dispersion to the truck. These findings collectively formulate the pollutant dispersion mechanisms behind an on-road truck as well as help pedestrians prevent from the harmful effects of vehicular emission.

Acknowledgment

This research is conducted in part using the research computing facilities and/or advisory services offered by Information Technology Services (ITS), The University of Hong Kong (HKU). Technical support from Ms. Lilian Y.L. Chan, Mr. W.K. Kwan and Mr. Bill H.T. Yau is appreciated. This work was supported by the General Research Fund (GRF) of the Hong

Kong Research Grants Council (RGC) RGC HKU 17210115 as well as the Environment and Conservation Fund (ECF) Project 26/2018 of the Hong Kong (HK) SAR.

References

Abdull, N., Yoneda, M. and Shimada, Y. (2020), "Traffic characteristics and pollutant emission from road transport in urban area", *Air Qual. Atmos. Health* **13**, 731-738.

Ahmed, S.R. (1981), "An experimental study of the wake structures of typical automobile shapes", *J. Wind Eng. Ind. Aerod.* **9**, 49-62.

Ahmed, S.R., Gawthorpe, R.G. and Mackrodt, P.A. (1985), "Aerodynamics of road and rail vehicles", *Veh. Syst. Dyn.* **14**, 319–92.

Anenberg, S.C., Miller, J., Minjares, R., Du, L., Henze, D.K., Lacey, F., Malley, C.S., Emberson, L., Franco, V., Klimont, Z. and Heyes, C. (2017), "Impacts and mitigation of excess diesel-related NO_x emissions in 11 major vehicle markets", *Nature* **545**, 467–471.

Baker, C.J. (2001), "Flow and dispersion in ground vehicle wakes", *J. Fluids Struct.* **15**, 1031-1060.

Benson, P.E. (1992), "A review of the development and application of the CALINE3 and 4 models", *Atmos. Environ. Part B. Urban Atmosphere* **26**, 379-390.

Berkowicz, R. (2000), "OSPM - A parameterised street pollution model", *Environ. Monit. Assess.* **65**, 323-331.

Cadle, S.H. and Stephens, R.D. (1994), "Remote sensing of vehicle exhaust emissions", *Environ. Sci. Technol.* **28**, 258-264.

Carpentieri, M., Kumar, P. and Robins, A. (2012), "Wind tunnel measurements for dispersion modelling of vehicle wakes", *Atmos. Environ.* **62**, 9-25.

Chan, T.L., Dong, G., Cheung, C.S., Leung, C.W., Wong, C.P. and Hung, W.T. (2001), "Monte Carlo simulation of nitrogen oxides dispersion from a vehicular exhaust plume and its sensitivity studies", *Atmos. Environ.* **35**, 6117-6127.

Chan, T.L., Luo, D.D. Cheung, C.S. and Chan, C.K. (2008), "Large eddy simulation of flow structures and pollutant dispersion in the near-wake region of the studied ground vehicle for different driving conditions", *Atmos. Environ.* **42**, 5317-5339.

Chang, V.W.-C., Hildemann, L.M. and Chang, C.-h. (2009a), "Wind tunnel measurements of the dilution of tailpipe emissions downstream of a car, a light-duty truck, and a heavy-duty truck tractor head", *J. Air & Waste Manage. Assoc.* **59**, 704-714.

Chang, V.W.-C., Hildemann, L.M. and Chang, C.-h. (2009b), "Dilution rates for tailpipe emissions: Effects of vehicle shape, tailpipe position, and exhaust velocity", *J. Air & Waste Manage. Assoc.* **59**, 715-724.

Cheng, W.C. and Liu, C.-H. (2011). Large-eddy simulation of flow and pollutant transports in and above two-dimensional idealized street canyons", *Boundary-Layer Meteorol.* **139**, 411-437.

Choi, H., Lee, J. and Park, H. (2014), "Aerodynamics of heavy vehicles", *Annu. Rev. Fluid Mech.* **46**, 441-468.

Clifford, M.J., Clarke, R. and Riffat, S.B. (1997), "Local aspects of vehicular pollution", *Atmos. Environ.* **31**, 271-276.

Davison, J., Bernard, Y., Borken-Kleefeld, J., Farren, N.J., Hausberger, S., Sjödin, Å., Tate, J.E., Vaughan, A.R. and Carslaw, D.C. (2020), "Distance-based emission factors from vehicle emission remote sensing measurements", *Sci. Total Environ.* **739**, 139688.

Dong, G. and Chan, T.L. (2006), "Large eddy simulation of flow structures and pollutant dispersion in the nearwake region of a light-duty diesel vehicle", *Atmos. Environ.* **40**, 1104-1116.

Giechaskiel, B., Riccobono, F., Vlachos, T., Mendoza-Villafuerte, P., Suarez-Bertoa, R., Fontaras, G., Bonnel, P. and Weiss, M. (2015), "Vehicle emission factors of solid nanoparticles in the laboratory and on the road using portable emission measurement systems (PEMS)", *Front. Environ. Sci.* **3**, 82.

Gosse, K., Gonzalez, M., and Paranthoën, P. (2011). "Mixing in the three-dimensional wake of an experimental modelled vehicle", *Environ. Fluid Mech.* **11**, 573-589.

Gong, L. and Wang, X. (2018), "Numerical study of noise barriers' side edge effects on pollutant dispersion near roadside under various thermal stability conditions", *Fluids* **3**, 105.

Habegger, L.J., Wolsko, T.D., Camaioni, J.E., Kellermeyer, D.A. and Dauzvardis, P.A. (1974), *Dispersion Simulation Techniques for Assessing the Air Pollution Impacts of Ground Transportation Systems*, Energy and Environmental Systems Division, Argonne National Laboratory, Illinois 60439.

Hu, X.J., Yang, H.B., Yang, B., Li, X.C. and Lei, Y.L. (2015), "Effect of car rear shape on pollution dispersion in near wake region", *Math. Probl. Eng.* **2015**, 879735.

Huang, Y., Organa, B., Zhou, J.L., Surawskia, N.C., Hong, G., Chan, E.F.C. and Yam, Y.S. (2018), "Remote sensing of on-road vehicle emissions: Mechanism, applications and a case study from Hong Kong", *Atmos. Environ.* **182**, 58-74.

Huang, Y., Ng, E.C.Y., Surawski, N.C., Yam, Y.-S., Mok, W.-C., Liu, C.-H., Zhou, J.L., Organ, B. and Chan, E.F.C. (2020), "Large eddy simulation of vehicle emissions dispersion: Implications for on-road remote sensing measurements", *Environ. Pollut.* **259**, 113974.

Hucho, W.-H., (1987), Aerodynamics of Road Vehicles: From Fluid Mechanics to Vehicle Engineering, 4th Edition, SAE International, Warrendale, USA, 956 pp.

Kanda, I., Uehara, K., Yamao, Y., Yoshikawa, Y. and Morikawa, T. (2006), "A wind-tunnel study on exhaust gas dispersion from road vehicles—Part I: Velocity and concentration fields behind single vehicles", *J. Wind Eng. Ind. Aerod.* **94**, 639-658.

Kang, Y., Ding, Y., Li, Z., Cao, Y., and Zhao, Y. (2017), "A networked remote sensing system for on-road vehicle emission monitoring", *Sci. China Inform. Sci.* **60**, 043201.

Kota, S.H., Ying, Q. and Zhang, Y. (2013), "Simulating near-road reactive dispersion of gaseous air pollutants using a three-dimensional Eulerian model", *Sci. Total Environ.* **454**, 348-357.

Lesieur, M., Métais, O. and Comte, P. (2018), *Large-Eddy Simulations of Turbulence*, Cambridge University Press, Cambridge, United Kingdom.

Liu, C.-H., Xie, J., Huang, Y. and Mok, W.-c. (2019), "Near-field vehicular plume mixing and roadside air quality", *The 15th International Conference on Wind Engineering* (*ICWE15*), September 1 to 6, 2019, Beijing, China.

Lo, K.H. and Kontis, K. (2017), "Flow around an articulated lorry model", *Exp. Therm. Fluid Sci.* **82**, 58-74.

Mazzoleni, C., Kuhns, H. D., and Moosmüller, H. (2010), "Monitoring automotive particulate matter emissions with LiDAR: a review", *Remote Sens.* **2**, 1077-1119.

McArthur, D., Burton, D., Thompson, M. and Sheridan, J. (2016), "On the near wake of a simplified heavy vehicle", *J. Fluids Struct.* **66**, 293-314.

Minguez, M., Pasquetti, R. and Serre, E. (2008), "High-order large-eddy simulation of flow over the "Ahmed body" car model", *Phys. Fluids* **20**, 095101.

Ning, Z., Wubulihairen, M., and Yang, F. (2012), "PM, NOx and butane emissions from on-road vehicle fleets in Hong Kong and their implications on emission control policy", *Atmos. Environ.* **61**, 265-274.

Owais, M. (2019), "Location strategy for traffic emission remote sensing monitors to capture the violated emissions", *J. Adv. Transport.* **2019**, 6520818.

Pospisil, J., Katolicky, J. and Jicha, M. (2004), "A comparison of measurements and CFD model predictions for pollutant dispersion in cities", *Sci. Total Environ.* **334**, 185-195.

Rao, S.T. and Keenan, M.T. (1980), "Suggestions for improvement of the EPA-HIWAY model", *J. Air & Waste Manage. Assoc.* **30**, 247-256.

Rohit, R., Kini, C.R. and Srinivas, G. (2019), "Recent trends in aerodynamic performance developments of automobile vehicles: a review", *Journal of Mechanical Engineering Research and Developments*, **42**, 206-214.

Sellappan, P., McNally, J. and Alvi1, F.S. (2018), "Time-averaged three-dimensional flow topology in the wake of a simplified car model using volumetric PIV", *Exp. Fluids* **59**, 124.

Tunay, T., Yaniktepe, B. and Sahin, B. (2016), "Computational and experimental investigations of the vortical flow structures in the near wake region downstream of the Ahmed vehicle model", *J. Wind Eng. Ind. Aerod.* **159**, 48-64.

Vino, G., Watkins, S., Mousley, P., Watmuff, J. and Prasad, S. (2005), "Flow structures in the near-wake of the Ahmed model", *J. Fluids Struct.* **20**, 673–695.

Wang, X.W., Zhou, Y., Pin, Y.F. and Chan, T.L. (2013), "Turbulent near wake of an Ahmed vehicle model", *Exp. Fluids* **54**, 1490.

Wang, Y.J., Nguyen, M.T., Steffens, J.T., Tong, Z., Wang, Y., Hopke, P.K. and Zhang, K.M. (2013), "Modeling multi-scale aerosol dynamics and micro-environmental air quality near a large highway intersection using the CTAG model", *Sci. Total Environ.* **443**, 375-386.

Weller, H.G., Tabor, H., Jasak, H. and Fureby, C. (1998), “A tensorial approach to computational continuum mechanics using object-oriented techniques”, *Comput. Phys.* **12**, 620-631.

Wen, Y., Wang, H., Larson, T., Kelp, M., Zhang, S., Wu, Y., and Marshall, J. D. (2019), “On-highway vehicle emission factors, and spatial patterns, based on mobile monitoring and absolute principal component score”, *Sci. Total Environ.* **676,** 242-251.

WHO (2020), World Health Organization Fact sheet: Ambient (outdoor) air pollution, World Health Organization, https://www.who.int/news-room/fact-sheets/detail/ambient-(outdoor)-air-quality-and-health (accessed on July 6, 2020).

Xie, S., Bluett, J., Fisher, G. and Kuschel, G. (2004), “On-road remote sensing identifies the worst vehicle polluters”, *Water & Atmosphere* **12**, 8-9.

Xing, Y. and Brimblecombe, P. (2018), “Dispersion of traffic derived air pollutants into urban parks”, *Sci. Total Environ.* **622**, 576-583.

Zhao, Y., Kato, S. and Zhao, J. (2015), “Numerical analysis of particle dispersion characteristics at the near region of vehicles in a residential underground parking lot”, *J. Disper. Sci. Technol.* **36**, 1327-1338.

Zhang, K. and Batterman, S. (2013), “Air pollution and health risks due to vehicle traffic”, *Sci. Total Environ.* **450**, 307-316.

Zhang, B.F., Zhou, Y. and To, S. (2015), “Unsteady flow structures around a high-drag Ahmed body”, *J. Fluid Mech.* **777**, 291-326.